Summer 7-31-2021

Study of halide gradient formation via solution-solid halide exchange in crystalline $CH_3NH_3PbBr_3$ thin films

Behnaz Akbari
University of Nebraska-Lincoln, bakbari2@huskers.unl.edu

Akbari, Behnaz, "Study of halide gradient formation via solution-solid halide exchange in crystalline $CH_3NH_3PbBr_3$ thin films" (2021). *Student Research Projects, Dissertations, and Theses - Chemistry Department*. 108.
https://digitalcommons.unl.edu/chemistrydiss/108

Study of halide gradient formation via solution-solid halide exchange in crystalline $CH_3NH_3PbBr_3$ thin films

By

Behnaz Akbari

A THESIS

Presented to the Faculty of
The Graduate College at the University of Nebraska
In Partial Fulfillment of the Requirements
For the Degree of Master of Science

Major: Chemistry

Under the Supervision of Professor Yinsheng Guo

Lincoln, Nebraska

July, 2021

Study of halide gradient formation via solution-solid halide exchange in crystalline $CH_3NH_3Br_3$ thin films

Behnaz Akbari, M.S.

University of Nebraska, 2021

Advisor: Yinsheng Guo

In this thesis, attempts have been made to understand halide exchange and mass transport inside the solid lattice of Lead Halide Perovskites (LHPs). We aim for the transformation of $MAPbBr_3$ using ionic solutions including 1-Butyl-3-methylimidazolium iodide (BMIMI), and 1-Butyl-3-methylimidazolium chloride (BMIMCl) as halide ion sources to observe the halide diffusion across the thin film sample and to have LHPs with a gradient of mixed halides ($MAPbBr_{3-x}(I/Cl)_x$, $0 \le x \le 3$). Successfully, $MAPbBr_3$ single-crystalline thin film was fabricated with different configurations. Surface analysis of the LHPs, elemental composition, halide diffusion, roughness, and size of grains in our thin film was examined using a scanning electron microscope equipped with Energy-dispersive X-ray Spectroscopy (SEM-EDX), photoluminescence (PL), and Dektak-XT stylus surface profiling system.

Acknowledgment

“*True teachers use themselves as bridges over which they invite their students to cross. Then, having facilitated their crossing joyfully collapse, “encouraging” them to create bridges of their own*.” “Nikos Kazantzakis”

I would like to thank my advisor, Professor Yinsheng Guo, his research group, and Professor Barry Cheung for their time during this research project.

My special thanks to Professor Patrick Dussault, the most influential, dedicated, honest, trustful, and understanding person who inspired me to pursue my goals. He has been always a wonderful resource of professional advice, and encouragement, beyond an advisor, to turn around obstacles into opportunities over the past two years at Chemistry Department.

I want to express my sincere appreciation to Professor Alexander Sinitskii for making all his good suggestions and feedback. I am greatly thankful to Dr. Thomas Smith for all his professional training, and cooperation. This project cannot be proceeded further without the supportive and professional guidance of the Physics Department, “Nebraska Center for Materials and Nanoscience”, as well. Therefore, I am immensely thankful to Dr. Shah Valloppilly, Dr. Balamurugan Balasubramanian, and Dr. Anandakumar Sarella for all their support, patience, and attention, providing me a positive learning environment to grow from their experience, and learn new techniques. I would appreciate my parents very much for their kind support, and all my true friends at UNL, especially: Laleh Abbasi (Post-Doc), Bo Zhang (Graduate student), Natalia Vorobyeva (Ph.D. candidate), and Parisa Sarzaeim (Ph.D. candidate).

Chap 1. Lead halide perovskites

- 1.1 Introduction
  - 1.1.1 LHPs (ABX3 composition, crystal structures, band structures)
  - 1.1.2 Photovoltaic performance and applications
  - 1.1.3 Optoelectronic applications
- 1.2 Overview of the electrical properties of LHPs
- 1.3 Progress in materials chemistry and its impact on optoelectronic properties and device performance
  - 1.3.1 LHPs with mixed cations (A)
  - 1.3.2 LHPs with Mixed anion (X)
  - 1.3.3 LHPs with Sn-Pb substitutions (B)
- 1.4 Overview of the solid-state chemistry of LHPs
  - 1.4.1 Halide exchange
  - 1.4.2 Ion migration
  - 1.4.3 Defect self-healing
- 1.5 Motivation of study
  - 1.5.1 Fundamental study of halide exchange and transport inside solid lattice
  - 1.5.2 If mesoscopic morphologies affect halide transport

Chap 3. Conclusion and Outlook

3.1. Summary of the LHP halide exchange experiments

3.2. Future Outlook

3.2.1 Fast halide exchange of Cl/Br co-insertion into the perovskite lattice thin films at room temperature

Abbreviations

Halide Perovskites (HaPs)

Light Emitting Diodes (LEDs)

Field-Effect Transistors (FETs)

Methylammonium (MA^+)

Formamidinium (FA^+)

Two-Dimensional (2D)

Zero-Dimensional (0D)

Quantum Dots (QD)

One Dimensional (1D)

Density-Functional Theory (DFT)

Gallium Arsenide (GaAs)

Charge-Coupled Devices (CCD) or (CMOS)

Image-Guided Radiation Therapy (IGRT)

Intensity Modulated Radiation Therapy (IMRT)

Indium Tin Oxide (ITO)

Doped Tin Oxide (FTO)

Mapbi$_3$ Photoconductors (MPC)

N-Type Hole-Blocking Layer (HBL)

P-Type Electron-Blocking Layer (EBL)

Polyimide (PI)

Organic LEDs (OLEDs)

Polymer LEDs (PLEDs),

Quantum-Dot LEDs (QLEDs)

Perovskite LEDs (PeLEDs)

Diffusion Length (LD)

Terahertz (THz)

Organic Photovoltaics (OPV)

Dye-Sensitized Solar Cells (DSSCS)

Photovoltaic (PV)

Metal Halide Perovskites (MHPs)

Power Conversion Efficiencies (PCE)

Methylammonium Iodide (MAPbI$_3$)

Methylammonium Lead Chloride (MAPbCl$_3$)

Methylammonium Lead Bromide ($MAPbBr_3$)

Electron-Dispersive Spectroscopy (EDS)

space-limited inverse temperature crystallization (SLITC)

X-ray photoelectron spectroscopy (XPS)

Chapter 1. Lead halide perovskites

1.1 Introduction

Lead halide perovskites (LHPs) have potential applications in the future optoelectronics, and electronics [1-7], because of their intrinsic electronic performance such as optimal bandgap [8-10], large absorption coefficient [11], high charge carrier mobility [12, 13], long carrier diffusion length [14, 15], long carrier lifetime [16, 17], small exciton-binding energy [18], low-cost materials, and facile synthesis methodology [1, 5, 7]. Perovskite materials have been rapidly developed for other applications beyond solar cells and photovoltaics [19, 20], namely, light-emitting diodes (LEDs) [21-25], photodetectors[26-29], lasers (such as 2D halide perovskites, and $CsPbX_3$ nanocrystal lasing [30-34]), memory devices [35-37] (such as halide perovskite quantum dots or resistive switching memory (ReRAM) with a composition of a metal-insulator-metal structure [38, 39]), and field-effect transistors (FETs) [40]. One of the interesting parts of research is using organic semiconductors in thin-film photovoltaics (PVs) [41], optical sensing, and X-ray detection [13, 14, 42-45].

The following sections provide a brief overview of the LHPs' composition, structure, and physical and chemical properties, and the synthesis approaches for fabrication processing.

1.1.1 LHPs (ABX_3 composition, crystal structures, and band structures)

The chemical formula ABX_3 is used to express a halide perovskite, where A indicates either a monovalent organic cation which can be methylammonium (MA^+) or formamidinium (FA^+) or an inorganic cation (Cs^+). The metal cation including Pb^{2+} or Sn^{2+} is corresponding to B, and the halide anion (I, Br, or Cl) is referred to as X. Five atoms exist in the unit cell of LHPs with the formula ABX_3 in the cubic structure which is also called single-phase. In this case, cation B poses six X anions closest to its neighbor, and the A cation has twelve closest neighbors. Moreover, crystallization of a perovskite crystal lattice, sharing BX_6 octahedral, occurs with a general ABX_3 (or equivalent) stoichiometry as indicated in Figures 1 and 2a. [1, 2, 5, 7]

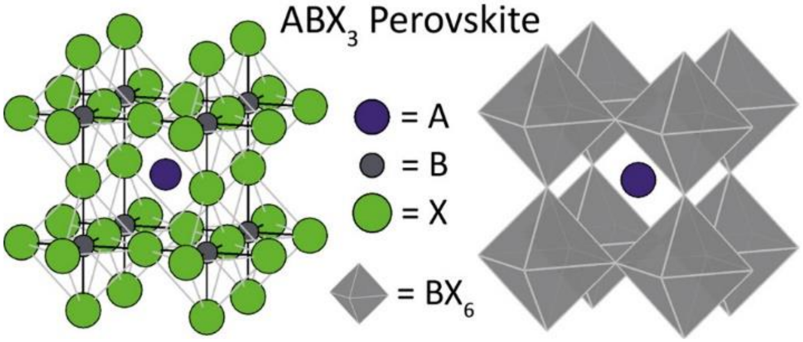

Figure 1. An aristotype cubic perovskite structure. Copyright permission from Chemical reviews [2] *Akkerman, Q.A. and L. Manna, What Defines a Halide Perovskite? ACS Energy Letters, 2020.* ***5****(2): p. 604-610.*

In 3D perovskite (ABX_3) stoichiometry, the **A** coordinates with 12 cations, and **B** is aligned to 6 X anions, leading to the formation of cuboctahedral and octahedral structures [2, 5]. Geometrically, a principle cubic architecture, the cell axis, "a", has a relation with the ionic radii (r_A, r_B, r_0). This is calculated by equation (1):

$$a = \sqrt{2} \times (r_a + r_0) = 2\,(r_B + r_0) \qquad \text{Equation (1)}$$

To estimate the degree of distortion, and compatibility of ion crystal structure, Golds Schmidt's tolerance factor (*t*) is introduced, and this is obtained by the ionic radii. This means that we would assume it as purely ionic bonding. However, this tolerance factor is considered as an indication for compounds with a high degree of ionic bonding; [6]. This assumption is defined by equation (2):

$$t = \frac{(r_A + r_B)}{\sqrt{2}(r_X + r_B)} \qquad \text{Equation (2)}$$

when we have a large A or a small B ion, *t* is larger than 1. So, it is expected that hexagonal variants of the perovskites have stability [7]. In general, the tolerance factor for stable 3D perovskite structures ranges from 0.76−1.13. However, the stability of other perovskite-related architectures does not share this same range. That is the reason why we have a limited number of A-cations such as Cs, MA, and FA which generate stable LHPs architectures. Other possible structures with A-cations which are too small (such as Na^+, K^+, and Rb^+) or too large (with imidazolium, ethyl ammonium, and guanidinium) are unstable[5]. It is essential to note that the tolerance factor must be close to 1 for a high-symmetry cubic configuration of perovskites within a range of 0.813 and 1.107.

The r_A, r_B, and r_X present the ionic radii of the related ions [1]. In LHPs, site B is usually occupied by Pb or Sn as large atoms; therefore, to meet the tolerance factor, site **A** must be sufficiently large. Otherwise, distortion of the cubic structure can occur, and we would see a decrease in the crystal symmetry. The measurement of tolerance factor for hybrid perovskites has remained a challenge as molecular cations need to be accurately assessed by their ionic radius. The LHPs commonly contain MA^+ and/or $HC(NH_2)^{2+}$ anions (FA^+) for site A. The crystal structure of $CH_3NH_3SnI_{3-x}Br_x$ perovskite and a comparison of the tolerance factors against other lead or tin halide perovskites are depicted in Figures 2a and 2b.

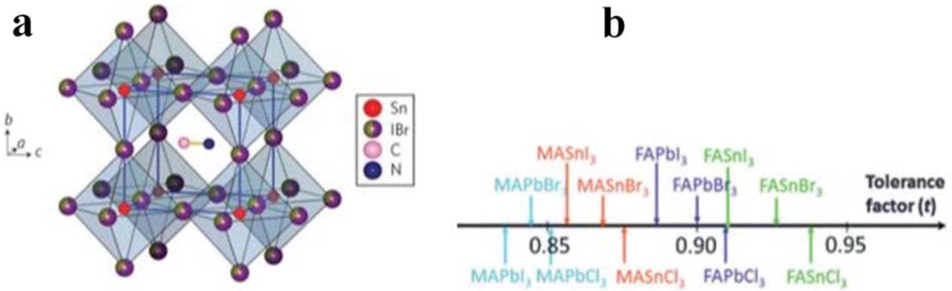

Figure 2. a) Crystal structure of $CH_3NH_3SnI_{3-x}Br_x$ perovskite **b)** Tolerance factor (*t*) of popular halide perovskites. Reproduced with permission. Copyright permission from Chemical reviews [1, 7, 46] *Jena, A.K., A. Kulkarni, and T. Miyasaka, Halide Perovskite*

Photovoltaics: Background, Status, and Future Prospects. Chemical Reviews, 2019. ***119****(5): p. 3036-3103.*

When site A is occupied by very large groups including a long chain of alkyl amine anions, LHPs are transformed to a two-dimensional (2D) layer structure[1, 5, 7].

The halide perovskites are considered direct-bandgap semiconductors, with bandgaps varying with composition and covering the whole visible spectrum. This family of materials also shows high photoluminescence quantum yield. For instance, it was reported that quantum yields for surface-treated $MAPbI_3$ perovskite thin films can be over 90% [7]. This report is critical as the charge carriers in the layers of perovskite materials can be an efficient way to produce in a photovoltaic device or a light emission device if it is recombinant. Tuning of the bandgap in a perovskite crystal can be done by altering the mixed halides (e.g., I–Br, Br–Cl), allowing for multicolor light emission devices and can be applied in any specific device with a certain bandgap[1, 9].

Theoretical studies have shown that the electronic structure of $MAPbX_3$ is dominated by the *p* orbital of X and the *p* orbital of Pb in the LHPs. Therefore, in general, the bandgap can be adjusted by the *p* orbital of X. In the $MAPbX_3$ perovskite materials, the valence orbitals vary from 3*p* to 4*p* to 5*p* when the X varies from Cl to Br to I. The optical absorption of $MAPbX_3$ single crystals (X = I, Br, Cl) also confirms the narrowing of the bandgap. This occurs when X is altered from I to Br which then changes to another halide, Cl. Several theoretical reports, confirmed by empirical reports, suggest that mixed (I, Cl) perovskites with high Cl content are difficult to form, while the formation of mixed (Br, Cl) as well as mixed (I, Br) alloys are easily achieved at room temperature [7, 47].

1.1.2 Photovoltaic performance and applications of LHPs

Research in perovskite photovoltaics, involving conversion of photons to electrons, and optoelectronics, involving conversion of electron flow to light, have evolved in an interrelated fashion, with applications in optoelectronic devices and optical sensing devices, both perovskite photovoltaics research and optoelectronics have evolved as a very interdisciplinary area where the conversion of a photon to electron exists and/or vice versa [48]. The outstanding photoluminescence properties of LHPs (particularly, those of $CsPbBr_3$) led to their introduction as the next generation of LEDs, and photodiodes [49-51]. Perovskite photodiodes have also been considered to use in color image sensing for digital cameras and medical diagnosis [48, 52-56]. Harvesting light with high efficiency is very important in optical management in devices made with thin photovoltaic films [53]. The excellent photophysical properties of organohalide perovskite as an intrinsic semiconductor and its impressive mobility of photo-generated carriers have been reported over the past few years [1, 5, 54-56].

The mechanism of photovoltaic activity involves charge generation, separation, and then diffusion of charge carriers to the electrodes [57, 58]. When illumination occurs, the absorption of photons by LHPs produces electron-hole pairs (or excitons which are bound states within the atomic lattice) in a few picoseconds. These electron-hole pairs pose binding energies that range starts from 19 to 50 meV which is low. This is similar to the thermal energy (*k*BT ~ 25 meV) when it is measured at ambient temperature. Therefore, the dissociation of excitons is facile and can further be facilitated by the large dielectric constant of halide perovskites. [54, 55].

Halide perovskites are semiconductors. One of the features that makes them so useful as devices are that tuning of the valence and conduction bands is easily accomplished [59]. Applications of density functional theory (DFT), and its calculations of the first principle theory have been incorporating with excellent photophysical properties of LHPs. This has been proved by optoelectronic measurements. As displayed in Figure 3, the band structures of $CH_3NH_3PbI_3$ are composed of the valence band (VB), containing a mixture of **I** 5*p* orbitals (~70%) and Pb $6s^2$ lone pair orbital (~25%), and the conduction band (CB) containing other orbitals, and Pb $6p^2$ orbital [48, 60]. Optical absorption and magnetoabsorption spectra of the LHPs materials have been studied by Kondo to clarify the impacts of halogens replacements measured by optical and magnetoabsorption. The excitons with the lowest energy in these crystals normally which have three-dimensional Wannier-type excitons were investigated along with the Bohr radii, binding energies, and oscillator strengths of the excitons with acceptable accuracy. It was concluded that the larger bandgap and having more tightly the natural band structure of the excitons in $CH_3NH_3PbBr_3$ in comparison with those crystals in $CH_3NH_3PbI_3$ is the intrinsic consequence of the substitution of halogens. There is a strong coupling between the Pb lone pair $6s^2$ orbital and the **I** 5p orbital, which are opposite to the electronic structure of gallium arsenide (GaAs) [61]. In the latter, the formation of VB and CB occurs by *p* orbitals and *s* orbitals, respectively. The *s* orbitals of the Pb lone pair and the symmetric orbital structure give rise to an outstanding high optical absorption coefficient for this type of perovskite (10^5 cm^{-1}) [62]. This contributes to the excellent photovoltaic property and production of high photovoltaic voltage [1].

The electronic properties of LHP perovskites are characterized by the diffusion lengths of electron carriers and their semiconducting nature. The long diffusion lengths of these carriers (between 1 µm for polycrystalline films [63] to over 100 µm for single crystals) [63] are explained by the defect tolerant nature of LHP perovskites [64]. The intrinsic semiconducting behavior of LHP perovskites is produced by the ambipolar nature of the carriers (such as in $CH_3NH_3PbI_3$) and the identical effective masses for electron and hole (0.23-0.29) in opposite to Si and GaAs [65]. Due to this nature, balanced charge transfer can be observed in the photoexcited state**.** Similarly, in the case of inorganic photovoltaic semiconductors, it is expected to observe that photogenerated carriers have free carriers in $CH_3NH_3PbI_3$. They can migrate in the absorber layers in the perovskite with no recombination if they are maintained for a long time [66, 67]. The photoluminescence measurements have shown that the lifetimes of these carries can be up to several hundreds of ns [25, 63, 68].

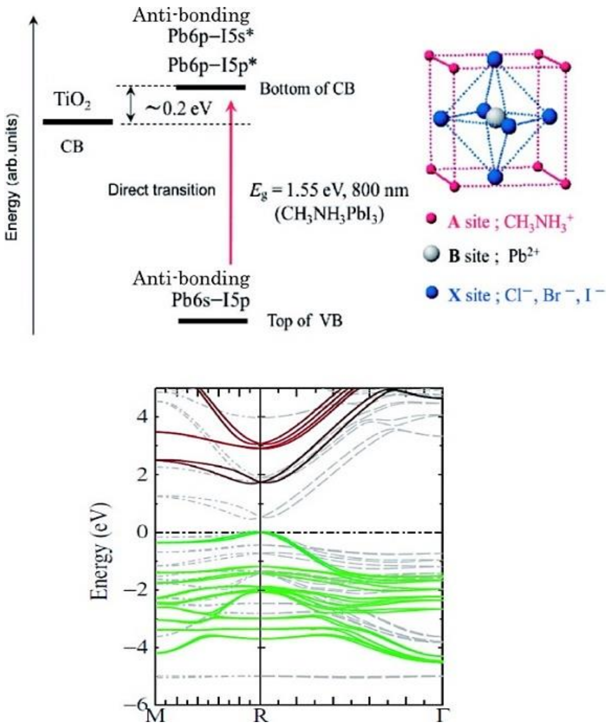

Figure 3. Depiction of the bandgap and crystal structure of $MAPbI_3$ as well as the energy diagram. The bottom shows bandgap architecture corresponding to the quasiparticle. [Zero: valence band maximum. Green solid line: **I** 5*p*; red solid line: **Pb** 6*p*; gray dot line: **Pb** 6*s*]. M and R: zone-boundary points. Reproduced with permission. Copyright permission from Chemical reviews.[48] *Miyasaka, T., Lead Halide Perovskites in Thin Film Photovoltaics: Background and Perspectives. Bulletin of the Chemical Society of Japan, 2018. 91(7): p. 1058-1068.*

1.1.3 Optoelectronic applications

Initial applications of LHPs have been concentrated on LEDs and transistors. However, as will be described below, the optical and electronic properties of these materials have led to a diverse set of applications [21, 22, 24, 33, 35, 49, 69, 70].

In addition to this, the optical and electrical properties of LHPs led to their consideration as potential sensitizing materials in dye-sensitized solar cells. Later, the creation of excellent separating charges as well as electricity, notable properties for charge transport, and a boosting absorption across the device led to the introduction of single-cell perovskite-based photovoltaic devices with high efficacy in the last few years [1-7].

As a result, the PCE of polycrystalline perovskite thin-film photovoltaic cells has improved from 3.8% to 23.7%. Compared to polycrystalline films, higher charge-carrier mobility, as well as longer diffusion length, have been seen in the materials, single-crystal perovskites that have no grain boundaries [1, 5, 7, 15]. This is because of their greatly decreased trap state density comparable with that of silicon and as a result, it is supposed to improve the device efficiency even further [1].

The potential applications of sensitive detection of X-rays include homeland security, medical diagnostic imaging, non-destructive methods for industry [13]. Sufficient sensitivity with a vast majority of active areas is required for these X-rays detectors. Currently, there are flat-panel detectors, non-flexible and detectors fabricated by expensive silicon materials, charge-coupled devices (CCD), or CMOS devices coupled with a scintillation layer [13, 71-73] are used in X-rays detection technologies. By introducing of scintillation layer, multiple imaging challenges occur which is pertinent to response times and signal-to-noise ratios [74]. The construction of a device with a large area based on flexible silicon is a challenge as well. Thus, it is recommended a flexible direct, real-time conformal X-ray detector; particularly, using flexible X-ray detectors that have been fabricated by a thin film. The shape of the object also is important to be considered in this case as spatial X-ray gradient is provided for image-guided radiation therapy (IGRT) and intensity-modulated radiation therapy (IMRT). In comparison with silicon materials used for X-ray applications, perovskite materials have a higher absorption coefficient than that of Si using in hard X-ray although μ_1 for 2D and 3D perovskites are identical. Within the two electrodes, fabrication of a highly crystalline thin film, and high charge transport and collection results in excellent X-ray absorption characteristics[75].

As shown in Figure 4, a detector incorporating a 0.83 mm X-ray absorber layer fabricated using a solution-processed perovskite displayed good sensitivity with X-ray detection [1]. It is interesting to note that the sensitivity of this device is an order of magnitude bigger than obtained in the indirect/direct detectors of TiCsI. Due to X-rays absorptivity, the detector must employ a layer of LHPs that is thicker than the layers used in the indirect/direct detectors. However, the ease of depositing perovskites from solution is predicted to facilitate detector preparation compared with the inorganic materials.

The thickness of the absorber necessitates having sintering [heating, pressure process to compact solid mass materials] at high temperature and vacuum deposition, etc. The former suggested semiconductor materials are more expensive than perovskite materials. Indeed, because of the chemical, and physical properties of the lead placed in absorber and X-ray, or γ-ray, as radiation detectors, future commercialization of perovskite materials is very bright. Although to achieve high sensitivity (high current response), high responsiveness in signal to noise ratio through dark background response suppression should be developed [53-56].

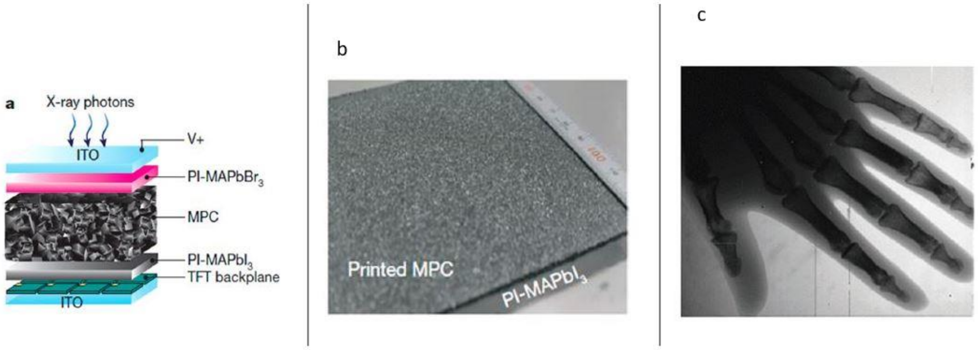

Figure 4. An X-ray detector fabricated by organic-inorganic perovskite absorbers. (a) image of processing all solutions utilized in digital X-ray detector. (b) illustration of printed $MAPbI_3$ photoconductors (MPC) on the polyimide (PI) PI-$MAPbI_3$. Indium tin oxide (ITO) is a conductive substrate. (c) image of a hand phantom X-ray gained from a detector. Copyright permission from Chemical reviews [1]. *Jena, A.K., A. Kulkarni, and T. Miyasaka, Halide Perovskite Photovoltaics: Background, Status, and Future Prospects. Chemical Reviews, 2019.* ***119****(5): p. 3036-3103.*

Among other applications, perovskites LEDs have gained interest as high luminance devices with low driving voltage [1, 5, 7]. LED technologies mobilized innovation for sustainable development and improvement of this device, namely inorganic semiconductor LEDs [76-81], organic LEDs (OLEDs) [82-85], polymer LEDs (PLEDs) [86, 87], quantum-dot LEDs (QLEDs) [88-93], and in the last decade, perovskite LEDs (PeLEDs) [8, 18, 49, 94-101]. A multi-layered PeLED device is composed of a front transparent electrode (typically doped tin oxide (FTO) or indium tin oxide (ITO)), an n-type hole-blocking layer (HBL), a back electrode, a p-type electron-blocking layer (EBL), and a perovskite emitter). To form a double-hetero junction structure, the perovskite active layer is inserted between the HBL and the EBL. This is performed for the confinement of the injected charges to have an efficient light emission. Once the voltage is applied through the transporting layers into the perovskite active layer, the electrodes inject charge carriers. This is the time for their radiative recombination, which led to emitting the light [96, 102-104].

1.2 Overview of the electrical properties of LHPs

The high absorption coefficient, long-range ambipolar charge transport, low exciton-binding energy, high dielectric constant, etc are critical physical properties of perovskite materials, [1, 17, 105, 106] for applications in optics[107] and electronics [8, 11].

The electrical mobility (μ) is the key factor in the electrical properties of Halide perovskites (HaPs). It is also considered as the drift velocity obtained by a charge carrier per unit of the applied electric field. Diffusion length (LD) is defined as the average distance when a charge carrier moves between generation and recombination. There have been several measurements for μ and LD in halide perovskites. Although several studies on $MAPbI_3$ have been reported thus far [108], there has not been agreement on a consistent set of values.

These inconsistencies may be attributed to purity, stoichiometry, and morphology differences of the samples, various construction pathways of perovskite materials[109-117], and different ways of measuring μ and LD[118]. The charge-carrier mobility of $MAPbI_3$ thin films, at room temperature, is reported to be between 8 and 35 $cm^2 \cdot V^{-1} \cdot s^{-1}$ [118-121]. There is no consensus on grain boundaries in the thin film. For thin films, it was astonishingly reported that the mobility of $MAPbI_3$ single crystals can cover an even wider range from 0.7 to 600 $cm^2 \cdot V^{-1} \cdot s^{-1}$[118, 122, 123].

Long carrier lifetime is a defining feature of high-performance photovoltaic devices with hybrid organic-inorganic perovskites [124]. It has been proposed that different microscopic mechanisms, including large polarons, Rashba effect [125, 126], and ferroelectric domains [127], and photon recycling [128] exist to produce this property. In addition to this, results showed that band-edge carrier lifetime rises once the system enters from a lower phase rotational entropy to a higher entropy phase. This leads to polarons formation[127, 129, 130], and extension of a lifetime [125, 127, 129-135].

Favorable charge carrier mobilities are known for MHPs from multiple processing paths [118]. The tunability of stoichiometry changes and the high value of charge-carrier mobility has been shown fundamentally as well. Typical values of charge-carrier mobility in the tens of cm^2/V s for lead iodide perovskites thin films along with these above-mentioned properties, and long charge-carrier diffusion lengths (in µm) under solar illumination densities were able to introduce a way for the fabrication of thin-film photovoltaic devices [63, 136, 137]. The charge-carrier mobility ratio and recombination rate have had a significant influence on the charge-carrier diffusion length. Although the trap concerning the rates of recombination is easily evaluated, charge-carrier mobilities have been just developed. Typical inorganic semiconductors, including GaAs, display only marginally lower effective masses for electrons of conduction band as well as valence band holes with noticeably higher mobilities.

Both the extrinsic and intrinsic effects can restrict the charge-carrier mobility in MHPs. Intrinsic effects are the consequence of the unavoidable interaction of charge-carrier with the fundamental lattice, permitting the well-designed high-charge-mobility MHPs according to the ABX_3 stoichiometry[58]. Extrinsic properties, however, are because of limited material defects, including grain boundaries, and energy disruption [3, 122].

1.3 Progress in materials chemistry and its impact on optoelectronic properties and device performance

Progress in materials chemistry has resulted in a significant increase in the long-term stability of LHP-based solar cells [1]. To enhance the stability, the combination of various cations at the A-site and various halides at the B-site were explored and successfully implemented. Successful compositional mixing to form a homogeneous solid solution does not occur always. However, with a certain mixture of cations at the A-site as well as halides at the B-site of the perovskites, the dominance of single-cation/halide perovskites has been demonstrated, resulted in either both efficiency or stability. According to the equation (1) and considering the parameters including size of the ion and geometrical tolerance factor, as the empirical index, to predict perovskite crystal structure, exploration of various cations and anions (I, Br, and Cl) or mixed have been conducted. The perovskites with quadruple cation, including Rubidium (Rb), considered as the fourth cation was proposed [7]. It was also revealed that Rb does not insert in any lattice site, instead, it is expelled out to grain boundaries [1, 97].

1.3.1 LHPs with mixed cations (A)

DFT calculations in all reported cases suggest that the iodine vacancy (V^{+}_{I}) has the lowest diffusion barrier, followed by MA vacancy (V^{-}_{MA}) and Pb vacancy (V^{-}_{Pb2}). However, the diffusion barriers were reported to scatter over a wide range of the quantitative results[1, 138]. Under DFT calculations[139], in LHPs, upon the interactions between the Pb 6*s*6*p and* I 5*p* orbitals, two bands will be produced: 1) the valence band maximum (VBM) through antibonding (σ*) Pb 6*s*−I 5*p* interactions; and 2) the conduction band minimum (CBM) through empty Pb 6*p* orbitals and/or by Pb 6*p*−I 5*p* interactions. Thus, the cations that are placed in the A-site do not have direct contribution toward the band structure. However, they can have a considerable impact on structural stability because the charge is compensated largely across the PbI_6 octahedra according to the interactions of their electrostatic (van der Waals) via the inorganic cage. In the lattice of the crystal, change in cations size, in the A-site can both contract and expand, leading to altering the perovskites' optical properties. Small cations in the lattice including Cs and Rb are predicted to contract the crystal lattice and therefore rises the bandgap. However, cations with large sizes such as FA+ are expected to expand the crystal lattice and reduce the band gap (E_g) [1, 5].

1.3.2 LHPs with mixed anions (X)

A mixture of various halides in the X-site has a powerful impact on optical and electronic properties, absorption and emission spectra, and carrier lifetime and diffusion length. several research reports claimed that sublimation of chlorine can easily occur out of perovskite materials such as $MAPbI_3$[140-142],; thus, Cl should not be retained in the ultimately formed film although the initial solution contains precursors of Cl ($PbCl_2$ or MACl)[143-146]. In contrast to this, it has been also supposed that $MAPbI_{3-x}Cl_x$ is a metastable phase with high formation energy and will not form a final perovskite film even though materials were started with Cl[147, 148]. Nevertheless, the quality and morphology of crystalline perovskite films are remarkably affected by Cl in the precursor solution [1].

$PbCl_2$ is considered as the additive source of Pb- or Cl-, including HCl[148, 149], NH_4Cl[150], and MACl[151], contributing to a high-quality film lacking pinholes when crystallization is slowed down. Consequently, the use of these additives during fabrication consistently increases device stability but also performance. The performance increases due to the greater diffusion length of electrons in $MAPbI_{3x}Cl_x$ in comparison with $MAPbI_3$ materials[151]. Though, as the carrier lifetime or diffusion length is related to polycrystalline films' morphology of (grain size and grain boundaries), separating the impact of Cl into electronic vs. morphology effects is challenging. XRD pattern studies showed that the gradual shift of Cl doping led to the dimensions of the crystal lattice cell. This progressively reduces when x is rising in $MAPbI_{3-x}Cl_x$ (x =0, 0.05, 0.1, and 0.3) single crystal materials at ambient temperature, showing that the $MAPbI_{3-x}$ Cl_x single crystal lattice architecture with a gradual change from the tetragonal phase to the cubic phase when X is rising.It is essential to mention that the inclusion and impact of Br in the X-site in the mixture of Br/I in perovskites materials affect directly directly affect both the optical or electronic properties. The smaller Br^- ions in $MAPbI_{3x}Br_x$ rises the bandgap of the mixed-halide perovskite once they are incorporated[152]. This increment in bandgap is because of a quadratic relation with Br concentration [1].

1.3.3 LHPs with Sn-Pb substitutions (B)

Stability issues attributed to LHPs solar cells (PSCs), and the toxicity of lead have been a major concern for industrialization, and commercialization, causing irreversible health effects [153, 154]. This issue led to investigations of perovskites that are lead-free or else incorporate a reduced amount of lead. A wide range of cations was introduced based on ionic size and Goldschmidt tolerance factor that estimates the perovskites' structural formability and stability to replace Pb. Group 14 elements, alkaline earth metals, transition metals and, lanthanides, and *p*-block elements can be suggested for replacing the perovskites without Pb. However, since we need to consider the stability in perovskite structure and photovoltaics factors, cations such as Sn^{2+}, Ge^{2+}, Mg^{2+}, Mn^{2+}, Ni^{2+}, and Co^{2+}, are the potential candidates for this aim[155]. This section discusses tin (Sn)-Based Perovskites as an example of lead-free perovskite. Tin has been chosen due to its similar ionic radii (1.35 Å) as of Pb^{2+} (1.49 Å). Tin-based perovskites offer a lower bandgap with higher charge carrier mobility (10^2–10^3 $cm^2 \cdot V^{-1} \cdot s^{-1}$) in comparison with their Pb analogs[156]. The exciton ionization is not restricted as most 3D perovskites with Sn showed binding energies (2−50 meV) comparable to that of Pb perovskites, because of the exceptional low effective masses[157]. Sn-based perovskites demonstrated several favorable optoelectronic factors compared with traditional semiconductors including CdTe and Si: narrow optical bandgap, absorption at wavelengths up to 1000 nm, bulk n-type electrical conductivity (5×10^{-2} $S \cdot cm^{-1}$), long diffusion length, as well as great electron mobility (~2000 $cm^2 \cdot V^{-1} \cdot s^{-1}$). However, the ease of oxidation of Sn^{2+} to Sn^{4+} at ambient temperatures poses a considerable challenge to application of Sn-based perovskites in PSCs [158]. If Sn^{4+} ion is oxidized, then, it behaves as a p-type dopant, resulting in the perovskites layer's self-doping, and PCE limitation. Sn perovskite films have also poor coverage, and inhomogeneity because of fast crystallization [159], resulting in numerous pinholes [160]. It was reported that different solvents can have effects on crystallization. Deposition from dimethyl sulfoxide (DMSO) as well as *N*-methyl-2-pyrrolidone (NMP) can give pinhole-free high-quality films, which is due to the induction of the intermediate phase, producing an extra ordinary rise in photocurrent, up to 21 mA/cm^2 [161]. Nonetheless, creating LHP material and devices with long-term stability still demands further investigations and remains as a challenge. [1]

1.4 Overview of the solid-state chemistry of LHPs

LHPs have rich and versatile solid-state chemistry. Replacement of one ion with another can cause distortions, and vary the lattice parameters as well as crystal symmetry at times[162]. This is because size differences occur between their placing and replaced ions[163]. The ideal cubic ABX3 perovskite is not very common and slight distortion of the mineral perovskites is often observed. Distorted perovskites have decreased symmetry are introduced for their magnetic and electric properties[164]. Goldschmidt et al in the 1920s pioneered structural studies on perovskites to explore the perovskite family of compounds.

1.4.1 Halide Exchange

The process of ion exchange in HaPs is related to the progression of a reaction in which structural ions are replaced by external ions [165]. Partial or complete ion exchange can result in the alteration of the crystal lattice [163]. Generally, the exchange process is conducted through either diffusion and reaction [163]. It was shown halide exchange can successfully occur in polycrystalline thin films by $MAPbX_3$ with X = Cl, Br, I) because the reaction was slow, and incomplete sublimation of $Br^-$by I^- is seen (Figure 5) [163]. This study proposed that size differences are the limiting factor. $MAPbCl_3$ and $MAPbBr_3$ have the cubic perovskite structure and $MAPbI_3$ has a distorted tetragonal structure. Therefore, for instance, in the $MAPbBr_xI_{3-x}$ system, the compound symmetry may alter once the halide exchange occurs. Another study reported that halide replacement in $MAPbX_3$ microcrystals with a predicted size of approximately 10μm with a morphology of an inverse opal can be obtained. A reaction of crystals of HaPs with gaseous hydrogen halide at higher temperature led to a complete halide exchange. Crystallinity and morphology were preserved for exchange with X, except in the case of having Cl− and I− where morphology is not retained. It was observed that their morphology is not maintained[163, 166]

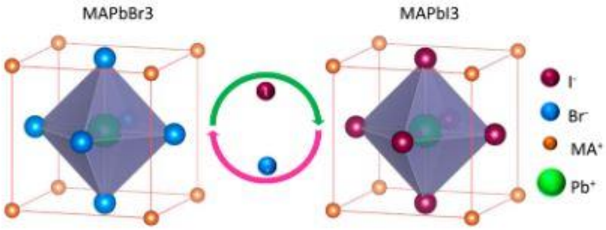

Figure 5. Illustration of reaction of reversible anion exchange across the LHPs. Reproduced from copyright permission [167] *Li, G., et al., Reversible Anion Exchange Reaction in Solid Halide Perovskites and Its Implication in Photovoltaics. The Journal of Physical Chemistry C, 2015.* ***119****(48): p. 26883-26888.*

In addition to this, halide exchange was studied to measure the halide drift as a driving force for exchanging the prototypical LHPs [163]. The initial step for halide exchange is the establishment of concentration gradients of ions across a span ranging from a few microns to a few hundred microns. From the surface, the depth of the replaced volume is based on how the halides have been paired. Which halide is exchanged, and exchanging is important to pay attention to. It was reported that the concentration gradient of the incoming halides reduces from the surface of the crystal toward its inner core and vice versa for the halides that are outgoing [163]. The gradient concentration varies slowly when the time changes with the crystal. Evaluation of halide diffusion coefficients can be functioned by the Boltzmann−Matano method. Also, diffusion profiles can be measured by electron-dispersive spectroscopy (EDS)[168]. It should be noted these parameters can vary, depending on the halide couple[163]. Moreover, while it was thought that gradients led to change in a lattice parameter and symmetry, X-ray diffraction showed that if the exchanged halides have identical size (e.g., $Br^-$and Cl^-, $Br^-$and I^-, but not $Cl^-$and I^-), the resultant perovskite materials will not alter single crystalline, and they would provide valid results irrespective of which halide is exchanging[163]. In the halide pairs that have a similar size, the solid-state chemical exchange is topotactic which determines the orientation of the crystal structure by that of the initial crystal, and explaining that substitution can occur through a topotactic reaction without damaging the single-crystal structure.

. As a result, crystal directionality is defined by knowing the initial crystal architecture. It was also examined that I−Cl exchange causes single crystallinity loss[169]. This contributes to a lack of miscibility, and it is thought to be a challenge to determine the presence of Cl in $MAPbI_3$ samples that were produced from solutions [163].

1.4.2 Ion migration

Ion migration is considered an intrinsic property of LHPs [168, 170]. This phenomenon occurs across the LHPs when an electric field is applied, causing perovskite solar cells' hysteresis (a unique characteristic of PSCs) and instability[171]. Also, determination of ion migration can be determined by impedance spectroscopy, galvanostatic measurement, photothermal induced resonance (PTIR) microscopy, and kelvin probe force microscopy (KPFM), as well as conducting atomic force microscopy (c-AFM).

In addition to this, ion transport is prominent for energy research. Devices such as batteries [172], fuel cells [138, 173], electrochemical sensors [174], and memristors include utilizing ion transport, relating to mixed conductivity. Conductors using mixed ionic−electronic materials have been extensively discussed in the area of solid-state Ionics, especially regarding the importance of oxide perovskites materials[175].

1.4.3 Defect self-healing

Given the nature of the perovskite materials, and because there are relatively soft ionic solids, a fundamental understanding of defect structures is essential[176]. “Self-healing” refers to the ability of a material to revert to its initial state once it is damaged by chemical, thermal exposure, or light conduction. It was reported that self-healing can occur inside the crystals of $MAPbBr_3$, $FAPbBr_3$, and $CsPbBr_3$ single crystals to repair and therefore minimize the two-photon absorption induced photodamage. Then, the photoluminescence recovery was monitored after the damage. It was shown that self-healing in $FAPbBr_3$ is the fastest (≈1 h) and in $CsPbBr_3$ is the slowest (tens of hours) for recovery. This is typical in the bulk, and dependent on degradation products' localization that is not far from the damage site[177].

The self-healing mechanism was explained with polybromide species that are present in the crystal, providing a closed cycle chemically. Due to the significant bond anharmonicity of halide perovskites crystalline, dynamic disorder across the well-defined crystalline lattice is also observed. It is noteworthy. that the efficacy loss observed when a solar panel is operated under illumination is reversed when the panel is kept in darkness. Nevertheless, When they are left in a dark place, recovery occurs [138].

1.5 The motivation of this thesis

In this thesis, we aim at understanding the fundamentals of halide exchange and transport inside the solid lattice of LHPs. We plan to achieve this objective by transforming $MAPbBr_3$ using an iodide solution to create LHPs with a gradient of mixed halides ($MAPbBr_{3-x}I_x$, $0 \leq x \leq 3$) and to map the chemical space of these materials.

Because the ion exchange is observed from the interface, studying halide exchange and transport helps us to have a good understanding of the solid-state of lattice behavior in this condition. Thus, in this study, attempts have been made to know how or which lattice degrees of freedom determine the halide transport. As we discussed earlier, 3D perovskite structures (ABX_3) stoichiometry poses the A and B cations and have coordination with 12 and 6 X anions, respectively. From the microscopic point of view, because of the octahedral structures of the halide perovskite with a 3D bonding network, we are interested in the motion of halide ions across the lattice.

Halide diffusion occurs inside the lead-halide octahedral bonded framework. It has been suggested that halide diffusion proceeds through this bonded network via halide vacancy. By studying the halide diffusion kinetics, we aim to identify key lattice degrees of freedom that dictate the ion transport inside the solid crystal.

The halide gradients formed in the halide diffusion study can be viewed as a chemical mapping of the composition space, translating the concentration of halides as a function of spatial coordinates.

The electrical and optical properties including optical absorption, and carrier diffusion lengths are defined by the chemical composition and lattice structure. In this research study, we design the chemical space mapping to directly expose the halide gradient. Accessible halide gradient maps will elucidate how halide perovskite optoelectronic properties vary concerning composition. This in turn enables high-throughput screening of desirable and/or unexpected materials behaviors.

1.5.1 Fundamental study of halide exchange and transport inside solid lattice

An effective method for changing the composition of raw material is performed via ion exchange, a chemical transformation method that maintains the original lattice structure of the LHP. [165]. As we discussed earlier, this reaction is typically done via ion diffusion that is kinetically managed with various ion concentrations between parent composition and reaction environments. Ion exchange has stood out in science because of the high tunability, and facile operability after synthesis to achieve heterogeneous architecture, core-shell structures, alloys, and metastable phase products. Because of the intrinsic softness ionic lattice of halide perovskites, modulation of physicochemical properties of halide perovskites is feasible to be investigated [178].

1.5.2 If mesoscopic morphologies affect halide transport

Another aspect of this study could be how mesoscopic morphologies affect halide transport. Diffusion coefficient magnitude is one of the important factors to consider in assessing halide transport. Reported values of halide diffusion coefficients vary by orders of magnitude for polycrystalline, single crystalline, and nano confined halide perovskites[163].

In addition to the above-aforementioned research motivations, it has been reported that the rates of ion migration are controlled by microstructure features, and this is different from bulk architecture [171, 178]. Consequently, decreasing the diffusion rate of grain boundary results in blocking ion diffusion if the boundaries are transverse to the electric field direction[179].

To develop methodologies to decrease ion migration and its effects, it is critical to know that whether we would have a homogeneous migration or if migration is influenced by microstructural characteristics including grain boundaries. By increasing the grain size, the charge that was accumulated starts decreasing, while the activation energies rise. This is coherent with the high grain boundary density in small-grained films accountable for easing charge transport [180].

We hypothesize mesoscopic interfacial structural features are responsible for such a wide span of diffusion coefficients. Halide perovskite interfaces such as grain and/or domain boundaries might support halide transport mechanisms that differ from that of the bulk. By comparing the kinetics of the halide exchange reaction between samples of varying heterogeneity, key differences of the thermodynamic variables affecting halide transport will be elucidated. Moreover, fundamental knowledge of the structural features defining halide transport in halide perovskites will lead to an advanced understanding of lattice defects, which will ultimately translate into improved materials properties and device performance.

Chapter 2. Halide exchange and diffusion in single-crystalline halide perovskite thin films

2.1 Introduction

Ion exchange, as a post-synthetic transformation approach, has shown to be able to control the compositions, and structures of materials beyond a synthetic pathway[181]. To resolve the kinetics on the single-particle level, few reports were made about the rich spatial and spectroscopic information. So, recently, image anion exchange kinetics quantitively was reported in nanoplates of individual single-crystalline LHPs through confocal photoluminescence microscopy (CPM) [181]. This symmetrical anion exchange route on the nanoplates is associated with the time of reaction as well as plate thickness which is monitored/controlled by the crystal structure and limitation in the mechanism of the diffusion of transformation[181]. Estimates based upon a reaction-diffusion model suggested the halide diffusion coefficient would be on the order of 10^{-14} $cm^2 \cdot s^{-1}$, resulting in 2D perovskite heterostructures. The spatially resolved coherent interface was realized via the reaction of anion exchange [181].

A recent study was conducted on $CsPbCl_3$–$CsPbBr_3$ single-crystalline perovskite nanowire heterojunctions to visualize directly the halide anion interdiffusion through wide-field and CPM measurements. Measuring intrinsic anionic lattice diffusivities was done by direct imaging techniques, free from microscale inhomogeneity. It was also reported that the halide diffusivities are in the range of 10^{-13} and $\sim 10^{-12}$ cm^2/second at around 100 °C [163]. This meant that the orders of magnitudes are several less than those reported for polycrystalline thin films [163]. Moreover, the key point of that study was the halide vacancies that facilitate ionic diffusion [163].

2.1.1 Review literature of halide exchange and diffusion

In halide perovskites, two procedures for ion exchange should be considered a) diffusion and b) ion exchange. Diffusion is the mass transfer, indicating that the ion exchange begins with interacting diffusion between the ions that are outside the investigated structure and ions that are components of the parent compound. This term is related to ions, molecules, and atoms when they are migrated in substances that are mainly coming from the thermal motion, and its kinetics are measured with Fick’s law. The volume of substance that has been diffused should be passed via the unit cross-sectional area if we want to have an ideal steady state of diffusion condition. This is a vertical diffusion direction that occurs per unit time (diffusion flux), and it is comparative to the concentration gradient at the cross-section:

$$J = -D\nabla C \qquad \text{Equation (1)}$$

where *J is* considered as diffusion flux, *D is* considered as diffusion coefficient, as well as *C* indicates concentration probably the number of atoms that have been diffused per volume, or the grams quantity per atom or any other units of the number in the substances The concentration distribution of diffused substances varies over time. According to Fick’s first law, concentration divergence and the continuity equation are combined to calculate Fick’s second law:

$$\frac{\partial C}{\partial t} = D \times \nabla^2 \times C \qquad \text{Equation (2)}$$

Fick’s law explains that the diffusion coefficient is the key parameter as it indicates the number of moles (mass) for the substance that has been diffused. Changes in concentration are perpendicular to the direction of the diffusion. This is calculated when the unit concentration gradient is considered per unit time. In practice, the diffusion coefficient *D* keeps follows the Arrhenius equation in a certain controlled temperature.

$$D = D_0 \times e^{-E_A/RT} \qquad \text{Equation (3)}$$

where D_o is considered a pre-exponential factor, R is equivalent to gas constant, E_A is a constant (diffusion activation energy), and T is known as temperature. Diffusion is nearly dependent on temperature. Different mechanisms can occur including atom migration in the lattice, vacancy diffusion, and interstitial diffusion mechanism[119, 165, 182-185].

In a halide perovskite, for instance, $MAPbI_3$, the intrinsic concentrations of I^-, Pb^{2+}, and MA^+ vacancies are expected to go beyond 0.4% at ambient temperature. This makes the main process of vacancy-mediated diffusion in $MAPbI_3$ perovskite materials [165]. Figure 1 depicts four types of mechanism for vacancy diffusion in halide perovskites.

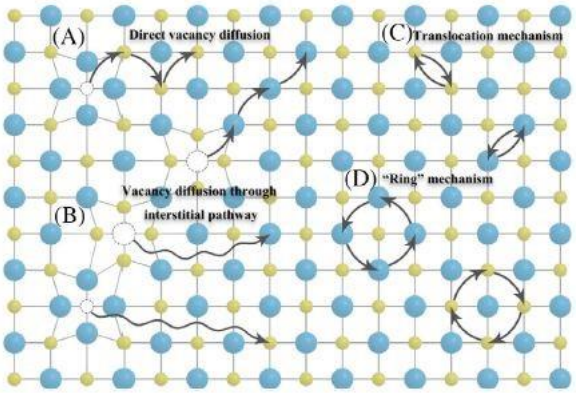

Figure 1. Vacancy diffusion. reproduced with a copy right permission[165]. Jiang, H., et al., *Ion exchange for halide perovskite: From nanocrystal to bulk materials.* Nano Select.

Apart from the constructed-covalent bond in MHPs, the A-site cation is also is part of an ionic link across the LHPs lattice but its migration is also affected by assisting such vacancy route[165, 186, 187]. Based on the above equation, several special factors having an impact on the ion diffusion of LHPs. These are described below:

2.1.1.1 Ion exchange in lattice sites

Diffusion of X-site halogen anions requires the least activation energy. This is due to the desirable vacancy-assisted diffusion. Migration of A-site cation engages movement via the unit cell face or bottleneck including four X-site ions. This results in the observation of higher activation energy compared to X-site anion. It is important to note that A-site cation occupies a significant fraction of the LHP unit cell volume, and its migration has a direct effect on the perovskite crystalline stability. The B-site ion is placed on the center of the cation sublattice architecture in perovskites, exhibiting the highest migration energy barrier. As for $MAPbI_3$, the activation energy at A site is 0.84, B site is 2.31, and X-site is 0.58 eV.[165, 187]

2.1.1.2 Reactions of Ion-exchange

Ion exchange occurs within the solution phase. The following steps present a process for understanding how cation and anion exchanges occur [165, 167]

$$\boldsymbol{ABX_3 + X'^{-}(sol.) \rightarrow ABX_2X'^{-} + X^{-}(sol.) \cdots\cdots \rightarrow ABX_3^{-}}$$

i. $ABX_2 - X \rightarrow ABX_2 + X\ (dissociation)$

ii. $X'^{-} \rightarrow X'\ (desolvation)$

iii. $3. ABX_2 + X' \rightarrow ABX_2 - X'\ (association)$

iv. $X \rightarrow X^{-}\ (solvation) \cdots\cdots \rightarrow ABX_3{}^{-\prime}$

This reaction shows that the cation exchange occurs in two steps (1 and 3), each of which can alter the crystal energy such as Born-Lande lattice energy as well as surface energy. Also, anion exchange reaction is related to the dislocation energies between the initial compounds (parent) and perovskites with product phases [188, 189]. It has been discussed that there is a decrease in crystal energy in product perovskite materials. This is led to a reaction of thermodynamically spontaneous ion exchange[190]. Ingoing cations and outgoing cations can be observed in step 2 (dissolvation) and step 4 (solvation) energies, relating to the ion solubility in the solvent. This is showing that the reaction continues to proceed once the ingoing cation is desolvated and the product cation is solvated. Therefore, by knowing the crystal lattice energy[165, 188], dissociation, interfacial strain energy [191], dislocation energy, [177], solvation energy [172, 188], and the thermodynamic aspects of the halide exchange reaction can be estimated[177, 188, 192]. In addition to this, the temperature of the ion exchange is highly important[165].

2.2 The objective of this study

In this work, attempts have been made to demonstrate how solution-solid chemistry using MAI and MACl solutions leads to the exchange of Cl and I into $MAPbBr_3$ perovskite thin films. Since the liquid-phase ion exchange has been discussed for bulk perovskite thus far and suffers from the contradiction that exists between ion source solubility compound and solvent polarity, we investigated the deposition of the MAI and MACl droplets on the single-crystalline perovskite thin film to improve the dissolubility, and the stability of MA-

X (X: Cl, and I) using the ionic liquid 1-butyl-3-methylimidazolium hexafluorophosphate (BMIMPF$_6$). The use of the ionic liquid enhanced not only the uniformity of the droplet on the MAPbBr$_3$ thin film, setting up a spatially controlled and spatially confined way to deliver a drop of halide ion solution, but also enabled complete halide exchange I and Cl with MAPbBr$_3$ was obtained. Additionally, chemical mapping on composition space was attempted to monitor halide gradient formation with different concentrations of MAI and MACl. Finally, a methodology of controlling the material composition to change structural dynamics and optoelectronic properties has been investigated.

2.3 Review literature on methods for LHP sample preparation - single crystal growth

This section reviews the fabrication techniques used for perovskite single-crystal thin films in detail. The overview is divided into three parts: i) solution-based lateral crystal growth; ii) vapor-phase epitaxial growth, and iii) top-down techniques [7, 57, 193-196]. In this thesis, we focus on solution-based growth of single-crystalline perovskite thin-film.

2.3.1 Synthesis of Bulk crystal

2.3.1.1 Antisolvent Vapor-Assisted Crystallization

Antisolvent vapor diffusion crystallization utilizes the different solubility behavior of perovskite materials in various solvents. In general, halide perovskites exhibit high solubility in DMSO, DMF, and GBL and low solubility in chlorobenzene, benzene, diethyl ether, etc. Those solvents with less solubility for LHPs are used as antisolvents with a slow diffusion into the precursor solution of perovskite (in DMSO, DMF, or GBL, etc.) until supersaturation of perovskite materials is reached and crystallization is induced. This technique is useful to grow large-scale bulk single-crystals, fabrication of single-crystal perovskite thin films via kinetic control or geometrical confinement can be performed (Figure 2).[197, 198]

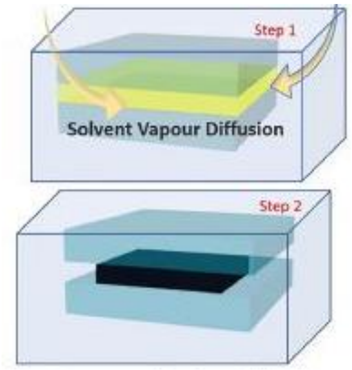

Figure 2. antisolvent vapor-assisted crystallization [193](reproduced with a copy right with permission 2021) *Hussain, I., et al., Functional materials, device architecture, and flexibility of perovskite solar cell. Emergent Materials, 2018. 1(3): p. 133-154.*

A study reported that a single-crystal $MAPbBr_3$ film could be fabricated through a cavitation-triggered asymmetrical crystallization approach [193]. The introduction of the transient ultrasonic pulse into a low supersaturation-level solution was done to induce non-symmetrical crystallization[193]. A single crystalline $MAPbBr_3$ film with a homogeneous and free of grain boundaries was achieved. Also, the thicknesses ranging from one up to several tens of microns and lateral dimensions changing from 100’s μm to 3 mm after several hours of crystal growth via dichloromethane vapor diffusion into the precursor solution were obtained. The drawbacks of this technique are size limitation, the formation of a (001)-oriented single-crystal $MAPbBr_3$ thin film, and a lack of generality in terms of applications to other halide perovskites[193, 199].

For the growing of the perovskite single-crystal thin films, antisolvent vapor diffusion crystallization in a confined space is also suggested, particularly for 2D perovskites. Single-crystal $(C_6H_5C_2H_4NH_3)_2PbI_4$ thin films with lateral sizes up to 1 cm with a minimum thickness of 1 μm via the diffusion of dichloromethane vapor into a solution of PbI_2 and $C_6H_5C_2H_4NH_3I$ in GBL over 30 min was fabricated, led to the introduction of a high compatibility method, and suggested for growth of another halide perovskite single-crystal thin films[193].

2.3.1.2 Retrograde solubility - inverse temperature

As the temperature increases, MHPs show decreasing solubility in certain organic solvents, such as DMF, DMSO, and GBL.[197] Accordingly, the perovskite-precursor solution can be heated to produce perovskite single crystals. The inverse solubility curve related to $MAPbI_3$ in GBL and $MAPbBr_3$ in DMF is shown in Figures 3a and 3b.

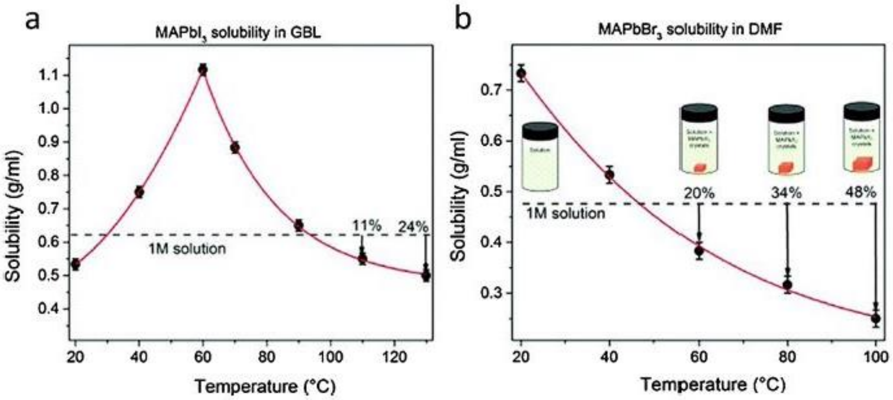

Figure 3. The solubility curves of (a) MAPbI3 in GBL and (b) MAPbBr3 in DMF (reproduced with permission. Copy right 2021[193]. *Wang, X.-D., et al., Recent Advances in Halide Perovskite Single-Crystal Thin Films: Fabrication Methods and Optoelectronic Applications. Solar RRL, 2019.* ***3****(4): p. 1800294.*

Initially, the formation of a complex was obtained by molecular binding of perovskites and solvent with low temperatures. Once the temperature increases, the complex is decomposed into free perovskite molecules [7]. Thus, heating a perovskite-precursor solution with the appropriate concentration can lead to effective inverse temperature crystallization. The crystallization rate of such a solution is an order of magnitude faster than that of other solution-phase techniques. Because of its simple procedure and fast crystallization rate, this technique is a common strategy for the fabrication of single crystals perovskite materials[152, 200-202]. Additionally, using two parallel plates for confined crystal growth along the z-direction with a controlled thickness, inverse temperature crystallization can be introduced to synthesize single-crystalline thin films [193](Figure 4).

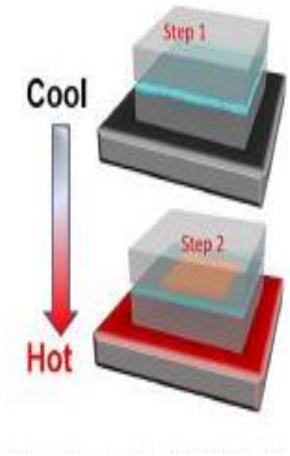

Figure 4. Inverse temperature crystallization (Reproduced with a copy right permission 2021)[193] Wang, X.-D., et al., *Recent Advances in Halide Perovskite Single-Crystal Thin Films: Fabrication Methods and Optoelectronic Applications.* Solar RRL, 2019. **3**(4): p. 1800294.

2.3.2 Growth of $MAPbX_3$ single-crystalline thin films

In the last few years, different bulk single-crystal perovskites have been fabricated, such as $MAPbBr_3$, $MAPbI_3$, and $CsPbBr_3$, and demonstrated as potential candidates for use in lasers, photosensors, X-ray detectors, and photovoltaic cells [7, 193]. The excessive thickness of the single crystals (longer than their diffusion length of charge carrier) and non-passivated surface defects have, however, severely restricted the development of optoelectronic applications based on the bulk single crystal perovskites[120, 127, 179, 203]. To overcome this barrier, the fabrication of large-area single-crystalline thin films is an effective approach to improve the optoelectronic efficiency of perovskite single crystals. It should be mentioned that single-crystalline perovskite thin films inherit the distinct properties of both polycrystalline films and bulk single crystals, such as low trap-site density, high mobility, and well-defined thickness. [193]

2.3.2.1 Solution-based growth of single-crystalline perovskite thin-films

The most widely used technique for preparing perovskite single crystal is solution-based growth. In general, this technique consists of two stages of nucleation and subsequent crystal growth, and as shown in Figure 5, both can be regulated using a solubility-super solubility diagram.

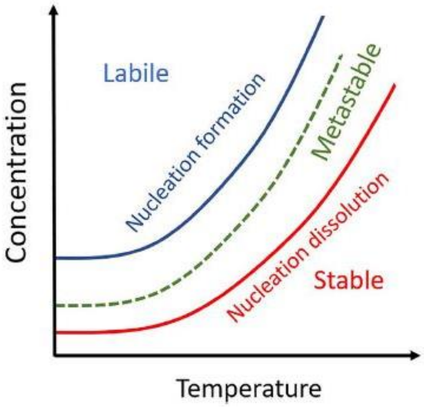

Figure 5. Solubility and super solubility (reproduced by copy right permission 2021 from WILEY-VCH Verlag GmbH and Co. KGA, Weinheim)[193] Wang, X.-D., et al., *Recent*

Advances in Halide Perovskite Single-Crystal Thin Films: Fabrication Methods and Optoelectronic Applications. Solar RRL, 2019. **3**(4): p. 1800294.

Different inverse temperature crystallization strategies that have been modified for single-crystalline thin films have been developed as shown in Figure 6. [193]

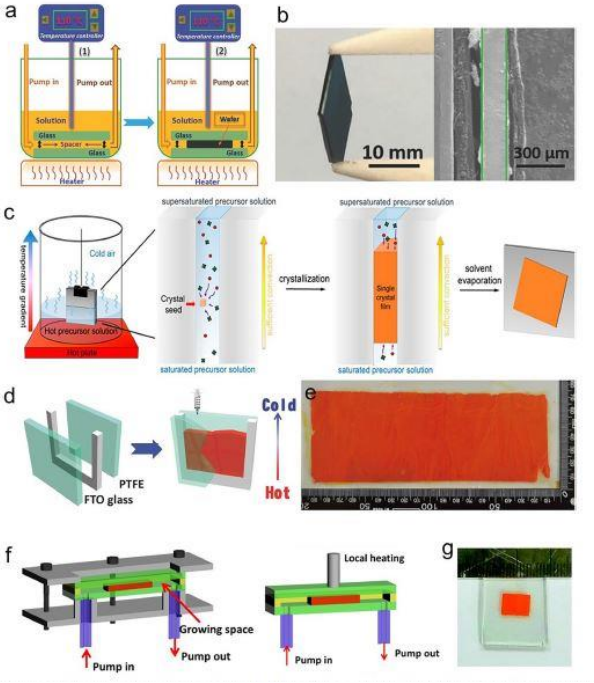

Figure 6. illustration of ITC methods for single-crystal perovskite thin films. a) thickness-controlled perovskite wafers b) SEM image of perovskite wafer c) various hybrid perovskites d) home-made spacer for growth of thin-film e) $MAPbBr_3$ crystal films (thickness:0.4mm) f) Flow cell g) FTO glass used for a laminar single-crystal $MAPbBr_3$ [193, 204-206]. For more information, please go to the reference [193] (Reproduced with Copy right permission (2021)) Wang, X.-D., et al., *Recent Advances in Halide Perovskite*

Single-Crystal Thin Films: Fabrication Methods and Optoelectronic Applications. Solar RRL, 2019. **3**(4): p. 1800294.

Based on the inverse temperature crystallization technique, a geometrically defined dynamic-flow reaction system for the growth of single-crystal $MAPbI_3$ wafers was developed as demonstrated in (Figure 6a). The dynamic flow was actuated using a peristaltic pump to effectively improve mass transport and facilitate continuous crystal growth by refreshing the solutions constantly. As can be seen in Figure 6b, using the sandwich spacers, the resulting single-crystal $MAPbI_3$ wafer had a comparatively large lateral size of about 1 cm with a controlled thickness of about 150 mm. Nevertheless, the wafers' excessive thickness prevents them from being used in a vertical structure solar cells and photodetectors. More recently, thinner single-crystal $MAPbI_3$ wafers that have 35 mm thickness were achieved using the same technique[193, 207].

For vertical structure optoelectronic devices, direct-grown perovskite single crystals on specific substrates are preferred over freestanding single crystals[208]. Submillimeter $MAPbBr_3$ single-crystal thin films on specific substrates (Figure 6c) were fabricated, in which two flat substrates were fastened together using the clips before being immersed into the perovskite-precursor solution vertically. By modifying the clipping force, the gap size between the two substrates could be modified, and thus, the resulting $MAPbBr_3$ crystal film thickness could be modified from 13 nm to 4.5 µm. Different successful perovskite single-crystal thin films grew on different substrates using this technique, such as quartz, ITO, Si, and PET. However, the single-crystal line perovskite thin films' lateral sizes were too limited (only hundreds of µm) to be effectively used in device fabrication[193, 204, 205, 209, 210].

Further study suggested an ingenious space-limited ITC technique[205]. An impressive, controlled 120 cm^2 large-area single-crystal $CH_3NH_3PbBr_3$ thin films with a thickness of 100–800 µm (Figure 6d and 6e) was obtained by the use of a spatially limiting platform compromising of FTO glass, a U-shaped thin polytetrafluoroethylene (PTFE) film, and a PTFE board. Furthermore, from bottom to top, a gradual reduction of temperature gradient was applied to control the crystal growth, and the precursor solution was constantly refreshed to obtain a large-area crystal growth. Another fascinating module (Figure 6f) was built based on a large lateral size (6 ×8 mm), and much thinner (16 µm) laminar $MAPbBr_3$ single-crystal films (Figure 6g). This was a successful design for having a minimum thickness of perovskite single-crystal thin film to 10’s of microns and organized with a peristaltic pump to aim for a fluid flow circulation of the precursor solution (MABr and $PbBr_2$ in DMF). Once the perovskite precursors are depleted, a fresh solution can replenish it with a steady flow. This enables to fabrication of continuous crystal growth, leading to a large-area perovskite single-crystal thin film. Furthermore, the employment of an ultrathin PTFE box for sealing the two glass substrates plays a pivotal role in the resultant perovskite single-crystal thin films’ thickness. For having a confined nucleation position, and simultaneous regulation of crystal nuclei, local heating at 90ºC was applied between the glass substrate[193, 205].

2.3.2.2 Microfluidic (1D) approach

Microfluidic and/or nanofluidic technologies have been an emerging technology in biological, biomedical, and biochemical research in the last two decades. Microfluidics is about how to manipulate fluids at the microscale (µl, nL, pL, or fL) to fabricate small, fast, and portable devices to decrease the time, and cost of analysis, and volumes of samples, and reagent [15].

Several materials are appropriate for the fabrication of microfluidic devices. Because of the low price, several protocols have been established for poly (dimethylsiloxane) (PDMS). This type of polymer is widely used in soft lithography and is biocompatible, gas permeable, and transparent, suitable for mass construction, PDMS suffers from surface modification properties over time, and hydrophobic substances are absorbed in its surface [15].

Several studies have been reported for the fabrication of 1D perovskite materials through microfluidic technologies. For instance, the growth of graph epitaxial liquid-solid nanowires of the photovoltaic materials $CH_3NH_3PbI_3$ in open nanofluidic channels was introduced via polar aprotic solvents. These wafer-scale perovskite nanowire thin films led to mm^2-sized surfaces comprised of perovskite nanowires in a controllable size, shape, and orientation manner [16].

In addition to this, laminar $MAPbBr_3$ single crystals were generated at a controllable thickness of 16 µm and size of 6×8 mm via space-limited inverse temperature crystallization (SLITC) growth [17].

Recently, a microfluidic flow cell has been published for microscopy applications and shows a passive flow control[211]. It has been found that thin flow-cell geometry can be combined with high numerical aperture (NA) optics to carry out high-resolution bright-field and fluorescence microscopies.

2.3.2.3 Other methods

1D aligned single-crystalline $CH_3NH_3PbI_3$ microwire arrays were reported to be fabricated through a simple solution-processed blade coating method at 100 °C. These microwires can be used in flexible sensors as novel optoelectronic devices including electronic eyes[7, 29, 41, 71], the implantable biomedical device[40, 212-216]s, and wearable electronics that had not been practical with rigid silicon-based image sensors[41, 71, 73]. An advantage of the chemical vapor deposition (CVD) method is precise surface, morphology, structure, and product composition control for the introduction of alternative synthesis pathway to obtain high-quality single-crystalline semiconductor nanowires although the difficulty of its direct use through this approach in the devices without manipulation and transfer has been reported[114, 208, 217, 218].

2.4 Experimental methods

2.4.1 Bulk crystal growth procedure of $MAPbI_3$ Single Crystals via Inverse temperature crystallization (for cuboids)

$MAPbI_3$ single crystals were fabricated by the inverse temperature crystallization method described by [219] with some modification. In brief, a 2:1 mixture of MAI (1.80 M) and PbI_2 (0.90 M) solutions in GBL (γ- butyrolactone) was sonicated for 10 minutes and filtered using a 0.22-μm PTFE filter. It should be noted that no evacuation and N_2 filtering were done in this method. It is also possible to shake the solution gently without sonication for 10 minutes. Then, the precursor solution in which 5 mL of clear, yellow $MAPbI_3$ solution exists, is distributed into two per closed vial. Then, it was placed in an oil bath at 60 °C for one hour. $MAPbI_3$ has the largest solubility at this temperature, and then gradually (1 °C per 20 min), the temperature increases to 135 °C. At this stage, the hotplate temperature should be slowly ramped from 60 °C to 135 °C to suppress nucleation and favor a slower growth rate to get larger grains. The time was adjusted to 24 hours to maintain the temperature at 135 °C. A single black $MAPbI_3$ cuboid grows on the bottom of the vial. Wiping off the harvested crystal can be done with filter paper Figure 7 (a).

2.4.1.1 Preparation of bulk $MAPbBr_3$ Single Crystals

Using the inverse temperature crystallization method, $MAPbBr_3$ single crystals were synthesized based on a modification of a known procedure [220]. A mixture of MABr (1.0 M) and $PbBr_2$ (1.0 M) in 5 ml DMF (*N*, *N*-dimethyl formamide- a polar solvent) was sonicated directly for 5 minutes and filtered using a 0.22-μm PTFE filter. The precursor solution is distributed into two vials (2 mL per vial). The transparent solution of $MAPbBr_3$ in a closed vial was placed in an oil bath at room temperature for 30 minutes. At this temperature, $MAPbBr_3$ has the largest solubility. To set up the program, the hotplate temperature should be slowly ramped from 25 °C to 100 °C for 24 hours for suppression of nucleation and controlling the experiment with a slower growth rate to obtain larger grains. Next, the temperature increases to 100 °C gradually (1°C per 20 min.). After almost 24 hours, it was observed that several $MAPbBr_3$ cuboids grew on the bottom of the vial and can be collected and wiped with filter paper Figure 7 (b).

2.4.1.2 Preparation of bulk $MAPbCl_3$ single crystals

High-quality $MAPbCl_3$ single crystals were fabricated by the inverse temperature crystallization method described in[206] with some modifications. Briefly, $PbCl_2$ (≥ 99.0%, 1.3905 g) and methyl-ammonium chloride (MACl) (98%, 0.3375 g, Aladdin) with an equimolar ratio were dissolved in a 2.5 mL of *N, N*-dimethylformamide (DMF) solvent and 2.5 ml of dimethyl sulfoxide (DMSO) solvent at 1:1 by a volume ratio at ambient temperature. Subsequently, the prepared solution was sonicated until no reactant precursor was presented. Next, filtration of the solution is done through the polytetrafluoroethylene (PTFE) filter with 0.22-μm pore size. For the growth of $MAPbCl_3$ single crystals, the precursor solution was transferred into some vials (1.5 mL per vial) and was kept in an oil bath. The temperature was set at 45 °C. The temperature of the oil bath was quickly elevated to 60 °C and maintained for ∼8 h. (Alternatively, the temperature could be increased from 45 to 60 °C at 1°C per 20 min.). It was observed that $MAPbCl_3$ single crystals with sizes of 2-3 mm were obtained. Notably, compared to the conventional one-step heating method, this two-step temperature process can generate $MAPbCl_3$ single crystals with high quality including a lower defect density. In addition to this, the low-temperature nucleation process at 45 °C plays a key role in obtaining the high quality of the crystalline thin film. Thus, the temperature of the hotplate should be slowly ramped from 25°C to 45 °C for 5 hours, and then from 45 °C to 60 °C for 8 hours to control the nucleation, resulting in slower crystal growth and larger grains Figure 7 (c).

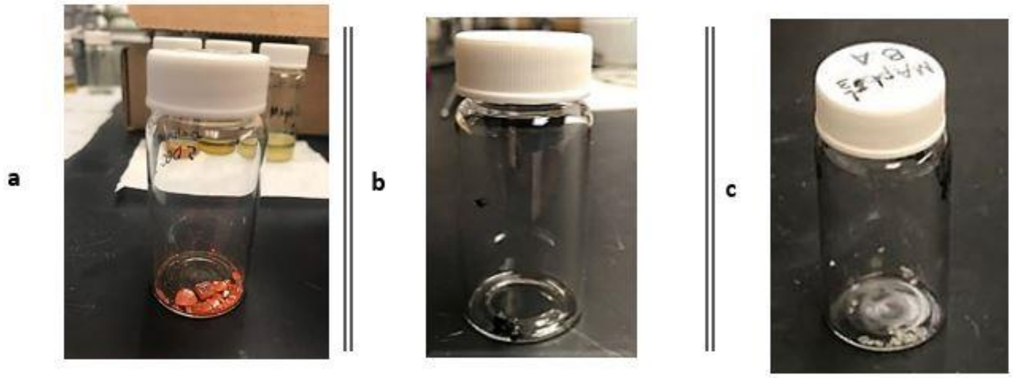

Figure 7. Bulk single crystals a) $MAPbBr_3$ b) $MAPbI_3$ c) $MAPbCl_3$

2.4.2 Space confined single-crystalline thin film growth methods for LHPs

2.4.2.1 Oversaturated Procedure for growth of single-crystalline $MAPbBr_3$ thin film

A mixture of MABr (1.0 M) and $PbBr_2$ (1.0 M) was dissolved in 2 ml DMF (*N, N*-dimethyl formamide), sonicated for 10 minutes, and filtered using a 0.22-μm PTFE filter. Glass slides were cleaned by IPA, and DI water in the ultrasonic bath for 5 minutes, and dried at room temperature. A U-shaped thin PTFE spacer was pre-patterned by a cutter. As displayed in Figure 8 (a-c), the flat substrates were assembled and clipped together. The clipped assembly confines growth space and reduces film thickness [208]. The temperature was slowly ramped programmatically, according to Rao's work [205, 208]. The precursor solution was replenished intermittently. millimeter-sized grains of $MAPbBr_3$ thin film was grown at the end of the growth procedure.

Various configurations of heat transfer and temperature control were implemented. Figure 8 shows the vertical placement of the crystal growth container for 24 hours. Figure 9 shows the vertically placed crystal growth carried out over multiple days. The temperature was slowly ramped to 60 °C for 30 minutes, and then ramped to 120 °C for 24 hours. On day five, the temperature was slowly ramped from 25 °C for 30 minutes to 80 °C, and maintained for 25 days.

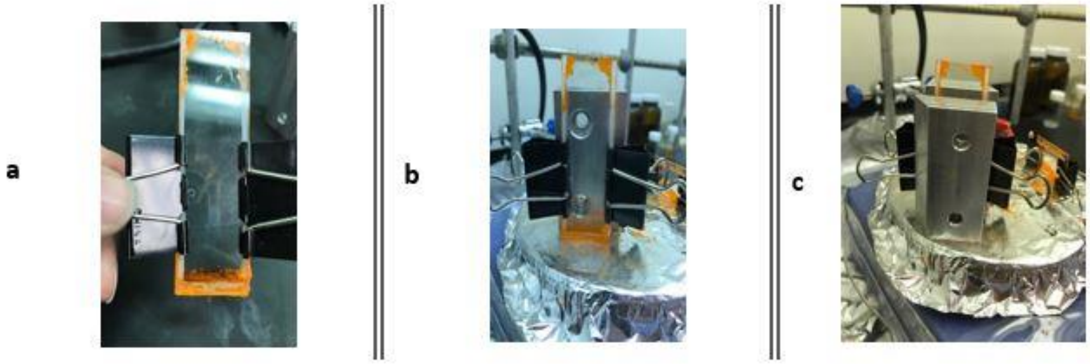

Figure 8. a) $MAPbBr_3$ crystalline thin film growth after 24 hours. b) New configuration of steel stack, PTFE, and substrate. c) demonstration of final configuration after starting the reaction.

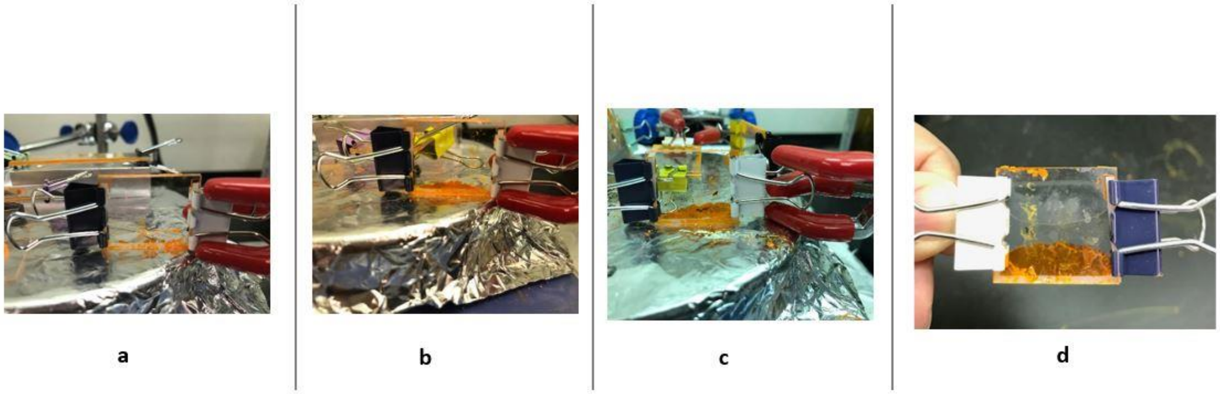

Figure 9. Photographs of the $MAPbBr_3$ crystalline thin film after a) 2 days, b) 5 days, c) 1 week, and d) 1 month

A planar configuration of heat transfer was implemented to grow $MAPbBr_3$ thin films, following a slightly modified procedure based on Rao's work [204, 205] (Figure 10). The temperature program was slowly ramped from 25 °C for 30 minutes to 80 °C. No crystal growth was observed initially for two days. The temperature was maintained at 100 °C for 5 days, better nucleation, and small grains of crystal thin films were observed. The precursor solution was not replenished during this attempt.

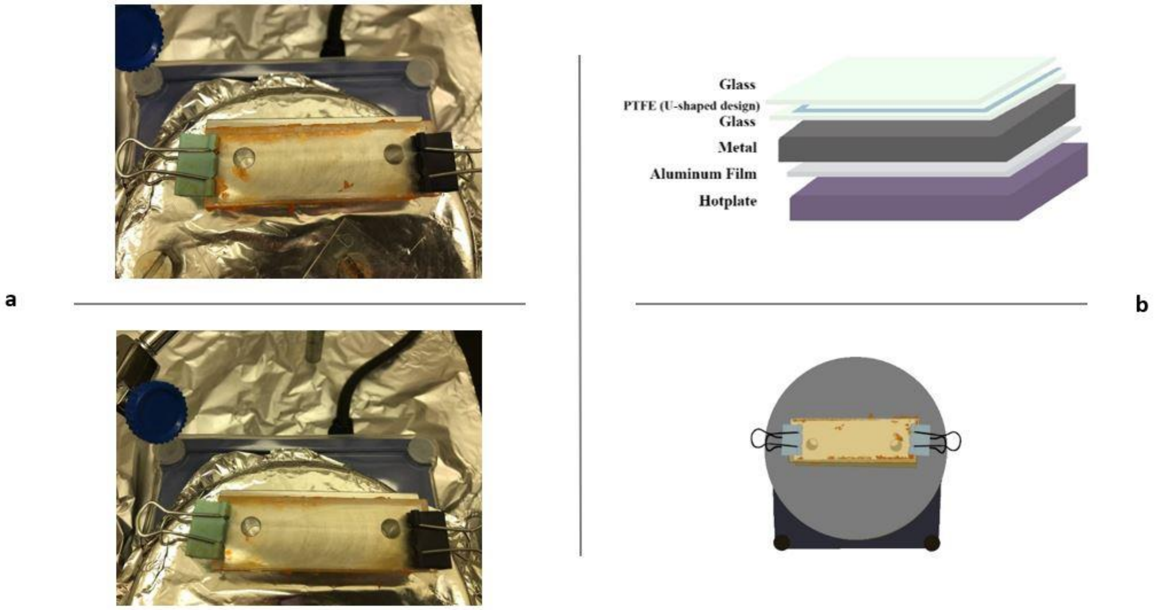

Figure 10. a) Photographs of $MAPbBr_3$ crystals. b) Schematic diagram of the new module for $MAPbBr_3$ crystalline thin film.

2.4.3 Introduction of ionic liquid solution as halide ion source

1-Butyl-3-methylimidazolium iodide (BMIMI), and 1-butyl-3-methylimidazolium chloride (BMIMCl) were selected as a halide ion source for their low vapor pressure/non-volatility, high ionic conductivity, and good thermal stability [221-223] to assess the halide diffusion-reaction on the MAPbBr3 single-crystalline thin film.

2.4.3.1 Quantitative procedures to prepare ionic solution as a halide ion source.

Efforts were made to dissolve MA-X (I or Cl) in ionic liquids (ILs), particularly with 1-butyl-3-methylimidazolium hexafluorophosphate ($BMIMPF_6$) to prepare a halide ion source solution for studying halide exchange.

2.4.3.1.1 Dissolution of Methylammonium iodide in 1-butyl-3-methylimidazolium hexafluorophosphate

Attempts have been made to introduce an optimized procedure for dissolution of methylammonium iodide (MAI) in 1-butyl-3-methylimidazolium hexafluorophosphate ($BMIM\text{-}PF_6$). 0.02 gr of MAI was added to 200µl of $BMIMPF_6$ corresponding to a concentration of 9.09 %W/W or 0.630M. The solution was sonicated at 50 ºC, and a bright yellow transparent solution was produced after 30 minutes.

2.4.3.1.2 Dissolution of Methylammonium chloride in 1-butyl-3-methylimidazolium hexafluorophosphate

Although several experimental procedures were conducted to dissolve MACl in $BMIMPF_6$, it was observed that MACl failed to dissolve at room temperature or even upon heating for 48 hours at 95 ºC. Stirring, sonication, and changing the concentration were not effective to disrupt powder agglomerates in this ionic liquid.

2.4.4 Solution delivery mechanism

First, a small droplet of halide ion solution was manually placed onto LHP thin film samples via disposable glass micropipettes with a minimal volume. The droplet was placed arbitrarily in the center of the $CH_3NH_3PbBr_3$ thin film under spatially confined growth conditions. Microcaps- Disposable Glass Micropipettes with a capacity of 10uL and single-channel Eppendorf pipettor with a volume range from 0.1 to 2.5µL were both used in this experiment (Figure 11).

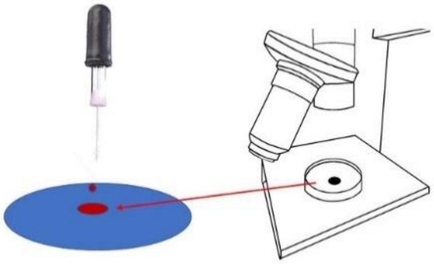

Figure 11. Schematics of microscope setup and use of microcaps with a 16 mm-length tip

2.4.5 Time-lapse imaging

Time-lapse imaging of $MAPbBr_3$ thin films was carried out on a home-built microscope. Low magnification large field of view objective lenses were used (Thorlabs AC254-150-AB, AC254-075-AB, and Nikon 10x Ph1-0.25-ADL). BMIMI or BMIMCl is deposited on MAPBBr$_3$ crystalline thin film under spatially confined growth conditions. Samples were monitored for a prolonged duration under ambient conditions.

2.5 Results and Discussion

2.5.1 Observed reaction phenomena

In the first attempt, we tried MACl and MAI dissolved in isopropyl alcohol (IPA) to study the diffusion coefficient for LHPs. However, as time changes, and once a droplet of MACl and/or MAI in IPA are placed on the MAPbBr$_3$ thin film, rings of MACl or MAI in IPA solution on the sample were shrunk, and then the solvents were evaporated. This limited our ability to measure the diffusion of halides on the thin film appropriately.

Thus, using ILs in this project was suggested due to their chemical, and physical properties, and considered as a better choice of chemical mapping, and diffusion study of halides.

2.5.1.1 Role of 1-butyl-3-methylimidazolium hexafluorophosphate (BMIMPF$_6$) in MAPbX$_3$ crystalline thin film

Figure 12 shows the halide solution droplet on top of a MAPbBr3 thin film. It is observed that the film morphology changed after being in contact with the droplet for 3 weeks.

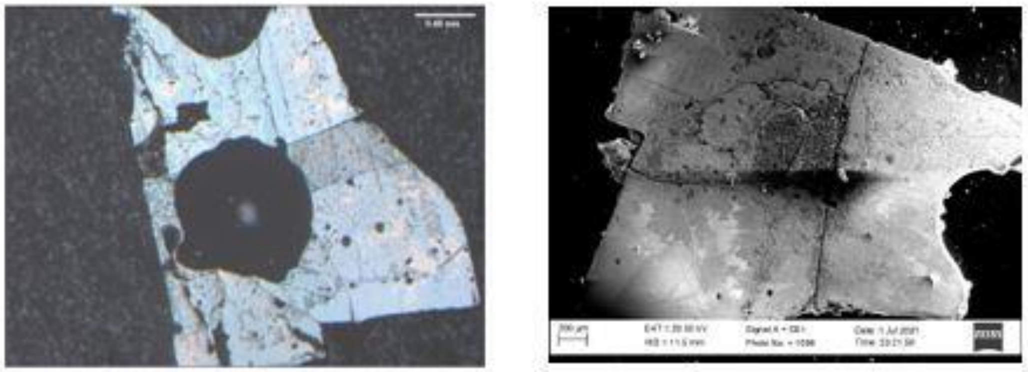

(a) (b)

Figure 12. a) microscopic observation of $MAPbBr_3$ after placing 0.1 µl of BMIM-PF_6 (Time: 0 (s)) b) the SEM image of the same $MAPbBr_3$ single-crystalline thin film sample for monitoring the halide transport after 3 weeks.

2.5.2 Characterization Techniques

2.5.2.1 Energy Dispersive Spectroscopy (EDS)

A scanning electron microscope equipped with energy-dispersive X-ray spectroscopy (SEM-EDX) is an analytical tool for measuring and spatial mapping the elemental composition of sample surfaces (X-ray mapping) [224]. During an X-ray mapping experiment in an SEM, the scanning high energy electron beam interacts with the sample and produces characteristic X-ray spectra that are unique to the elements present in the locally scanned region [225]. This technique can potentially be applied to and map the distributions of elements of interest including Pb, C, Cl, Br, and I on the surface of

$MAPbBr_3$ crystalline thin films and thus the diffusion of halides in our study. Particularly, the line profile of EDX mapping can be used to determine the local elemental composition of the surface taken perpendicular from the rim of the ionic liquid droplet on the top of the perovskite film samples discussed in previous sections to areas away from the droplet. Changes in the elemental compositions along this line profile can indicate the degree of halide diffusion.

In our preliminary experiment, to evaluate the halide diffusion using the SEM-EDX technique, we placed a 0.1-μL droplet of BMIMCl on a $MAPbBr_3$ crystalline thin film (Fig. 13). To accelerate the discussion of chloride ions into the film, the sample was heated at 50 ºC and the resulting sample was analyzed using line profile elemental mapping. We observed that the droplet of BMIMCl deposited on the surface of $MAPbBr_3$ crystalline thin film did not evaporate at room temperature. Also, the color of the placed droplet turned brown after the heating. It should be mentioned that the melting point of BMIMCl (salt) is 41 ºC [226]. If halides exchange between the BMIMCl and the $MAPbBr_3$ thin film, we expect that mixed halide perovskite (such as $MAPbBr_{3-x}Cl_x$) may be detected across the sample.

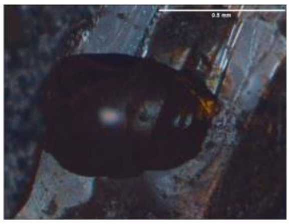

Figure 13. Photo of a 0.1-μL droplet of BMIMCl on a $MAPbBr_3$ crystalline thin film.

Figure 14 (a) shows the EDX spectrum of the region of our interests. The EDX line profile indicates the presence of Pb and Br along with the very small concentration of Cl at this location (Figure 14b). Figure 14 (c) shows an SEM image of a $MAPbBr_3$ film sample with a dried droplet of BMIMCl placed near the top-right of the thin film. The droplet is indicated by a darker gray circle. The sample was heated at 50 ºC for 30 min. At the rim of the droplet, an EDX line scan was performed along the red line. . The data suggests that SEM with EDX mapping and spectra along lines can be potentially applied to investigate the diffusion halide from the BMIMCl droplet across the $MAPbBr_3$ film and yield information of halide gradients over multi-micron length scales in our study. To verify the incorporation of the chloride in the lattice of the $MAPbBr_3$ film to form mixed halide perovskite ($MAPbBr_{3-x}Cl_x$), the use of X-ray photoelectron spectroscopy (XPS) can be further explored in future studies. Figure 14 (a) shows the EDX spectrum of the selected region of our interests. SEM image of the $MAPbBr_3$ crystalline thin film and EDX spectrum of BMIMI placed in the center of a MAPbBr3 film sample with its spectra have been showing in Figure 15. The droplet is shown by a darker gray circle. The sample was heated at 50 ºC for 120 min. An EDX line scan was performed along the red line within the sample. The EDX line profile demonstrates the presence of Pb and Br along with the very small concentration of I at this location (Figure 14b). The data suggest that SEM with EDX mapping and spectra along lines can be ideally applied to study the diffusion halide from the BMIMI droplet across the $MAPbBr_3$ film and yield information of halide gradients within the sample in micron length scales in this project.

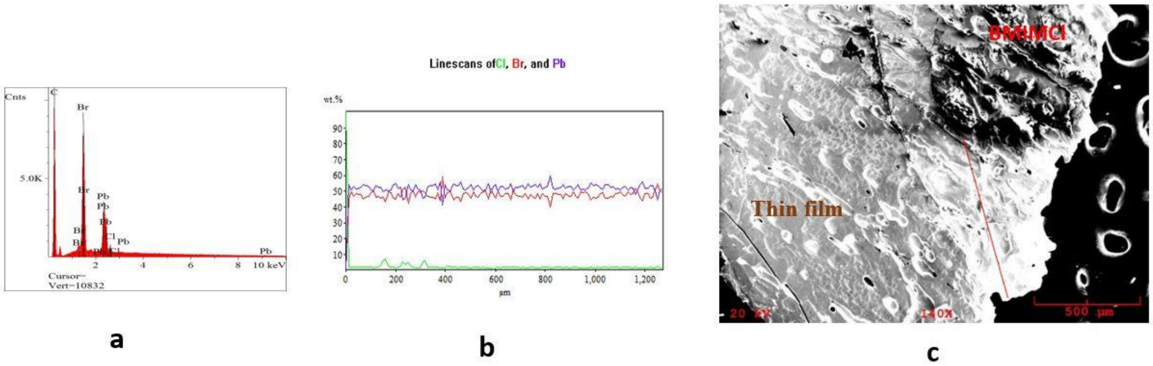

Figure 14. SEM-EDX analysis of a $MAPbBr_3$ crystalline thin film with a dry droplet of BMIMCl after 30 min. of heat treatment. (a) EDX spectra in a certain region. (b) EDX line profile of Pb, Br, and Cl along the red line in (c). (c) SEM image of the $MAPbBr_3$ crystalline thin film. The darker gray circle indicates the location of the dried droplet at the top-right of the thin film.

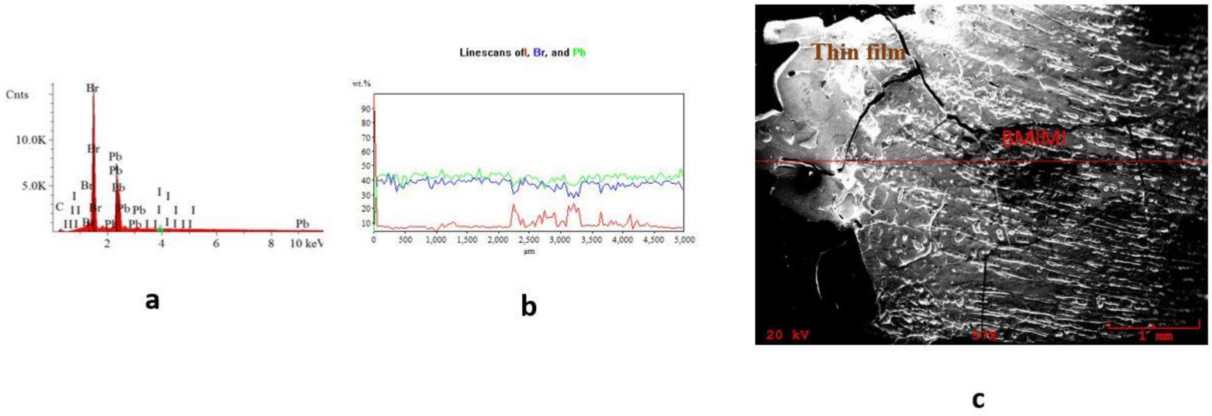

Figure 15. (a) EDX spectra in the certain region (b) EDX line profile of Pb, Br, and I along the red line in (c). (c) SEM image of the $MAPbBr_3$ crystalline thin film. The darker gray circle indicates the location of the dried droplet at the center of the thin film.

2.5.2.2 Photoluminescence spectroscopy

Photoluminescence spectroscopy (PL) is a non-contact, non-destructive approach to detect the molecular and structural changes for materials including solids, solution, solid suspensions, and gaseous. The sample is exposed to a light source (usually a laser) and absorbs light (photo-excitation stage), resulting in the formation of electronically excited states. Subsequently, the energy is released, and the materials return to the ground state with the emission of light. PL fingerprints can identify various defect states by PL either at higher or especially at lowest temperatures [121, 227] and investigate the perovskite materials in different environments including solvent, humidity, or atmosphere[228].

In our study, a laser operating at 532 nm was used to excite the $MAPbBr_3$ in the PL measurements. The laser beam of 2.5 mW power was focused on the $MAPbBr_3$ surface. The arbitrary area of the sample was chosen and imaged by a CMOS camera. Photoluminescence was collected by the same objective, sent into a spectrometer, dispersed by a 600 gr/mm grating, and recorded by a cooled charge-coupled device (CCD) detector operating at -70^{oC}.

2.5.2.2.1 Photoluminescence measurement on $MAPbBr_3$ crystalline thin film

Photoluminescence (PL) of the MAPbBr3 crystalline thin films with a deposited BMIMI was performed to seek any evidence of mixed halide perovskite, resulting from halide exchange and showing shifted PL. Two types of samples were used. 1) IL droplet (here is BMIMI) on LHP film sample (in which X ion solution and LHP have been in contact for prolonged time) and 2) pristine LHP film (as control).

Multiple locations on the sample surface with varying distances to the solution-slide interface were examined for meaningful variations in the PL spectra. The optical images of pristine $MAPbBr_3$ perovskite thin films with and without the laser spot at room temperature have been collected, as well as images of $MAPbBr_3$ perovskite thin films after adding 0.1 µl of BMIMI at room temperature with/without a laser spot location (Figure 15 (a) and (b)). The total experimental reaction of BMIMI-$MAPbBr_3$ crystalline thin film was 2 minutes. The shifted PL were all taken at a fixed grating position of 540 nm using a 600 g/mm grating. The exposure time to laser was 0.05 s. Next, the PL of $MAPbBr_3$ crystalline thin film during the reactions of halide exchange (here is BMIMI) was collected at several locations.

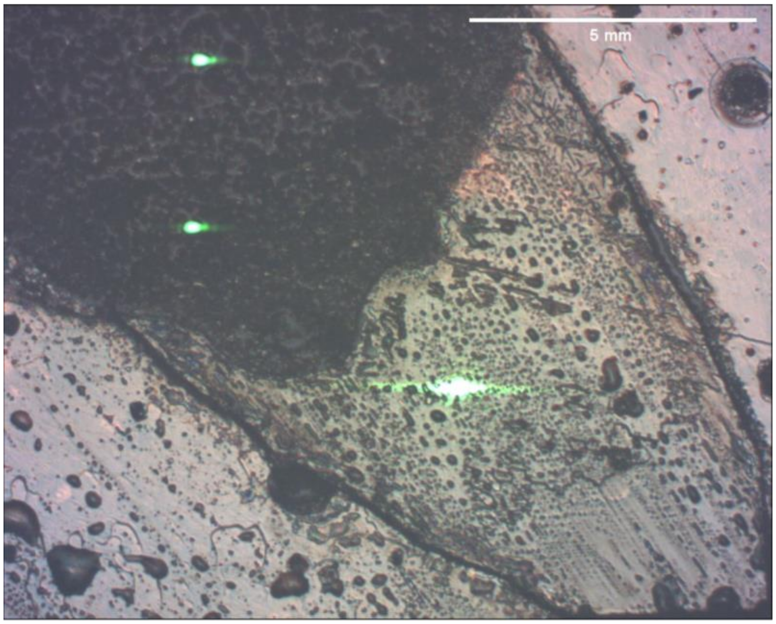

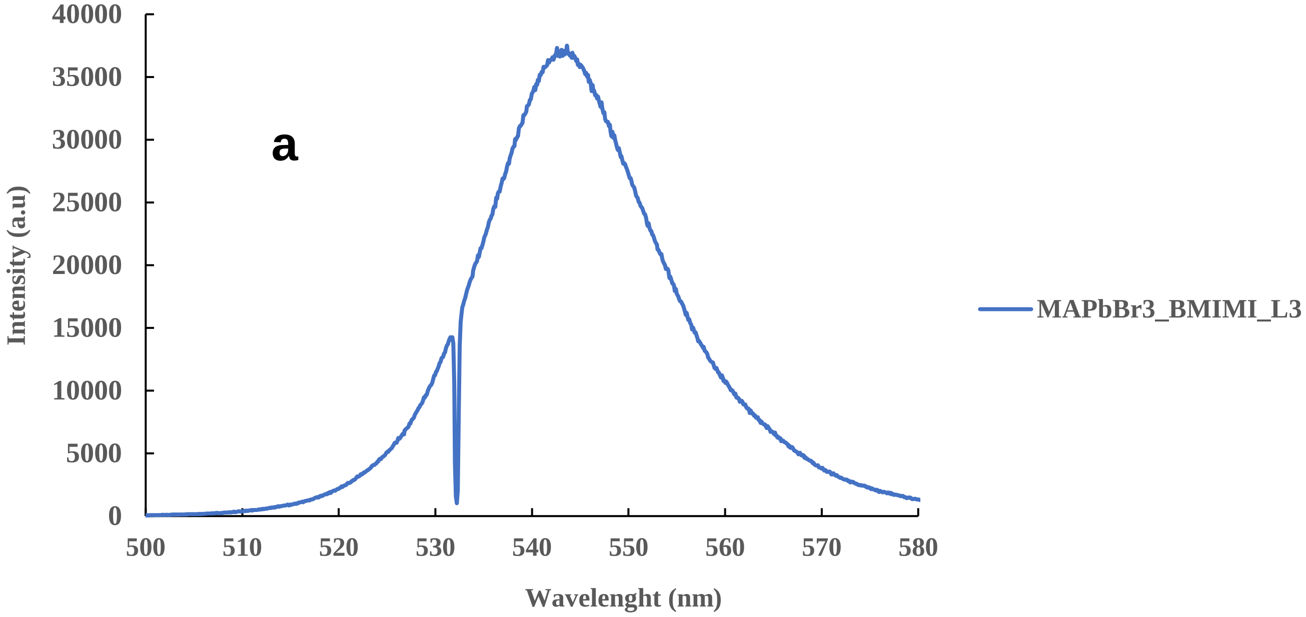
a
Intensity (a.u)
0
5000
10000
15000
20000
25000
30000
35000
40000
500
510
520
530
540
550
560
570
580
Wavelenght (nm)
MAPbBr3_BMIMI_L3

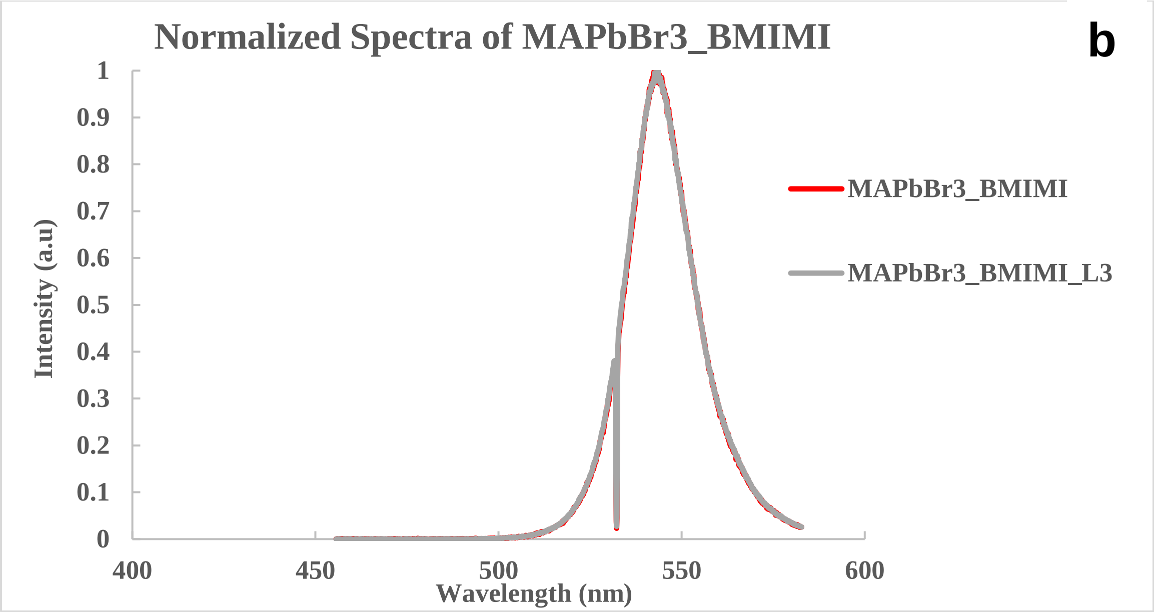

Figure 15. a) Selected PL spectra for MAPbBr3-BMIMI at the selected location (L4) surrounding the BMIMI droplet with corresponding image b) Overlay of normalized PL spectra of MAPbBr3-BMIMI at room temperature, different locations, and different distances

Significant peak shifts were not observed from solution-solid halide exchange experiments as indicated in Figure 15 (b). Spectra collected from different locations exhibited essentially identical peak position and width as shown in Figure 16, with varying intensities.

As a further attempt, 0.1 µl of BMIMI was deposited on the center of $MAPbBr_3$ crystalline thin film and then was placed in the oven to dry over 1 hour at 50 ºC. Full scan analysis of $MAPbBr_3$ and $MAPbBr_3$ -BMIMI for any composition or anion exchange conducted by PL measurement showed that no spectral variations were seen.

The PL data is correlated to the SEM-EDX results, both showing the absence of a halide gradient. One may continue the experiment at room temperature or at a higher temperature for a prolonged duration to investigate if there is any pair halide after adding BMIMI or BMIMCl.

2.5.2.4 Profilometry

As depicted in Figure 17 (a), and (b), a Dektak-XT stylus surface profiling system was used to probe different locations on the thin film surface, profiling film thickness (depth) while walking on the $MAPbBr_3$thin film surface. As given in Figure 17 (c), the plot, initially, was flat, corresponding to the substrate (glass), and then was increased sharply to 118.1570 µm since it probes the surface of $MAPbBr_3$ crystalline thin film sample. This is followed by less fluctuation from 118.1570 µm once the probe position is in 1073.1329. Finally, the average total profile for the measurement of the thickness is 115.8454 after 3 times analysis. This obtained thickness is aligned with the proposed method for fabrication of single crystal thin film by ITC described by Rao et al.[193], ranging from 100-800 µm for $MAPbBr_3$ material.

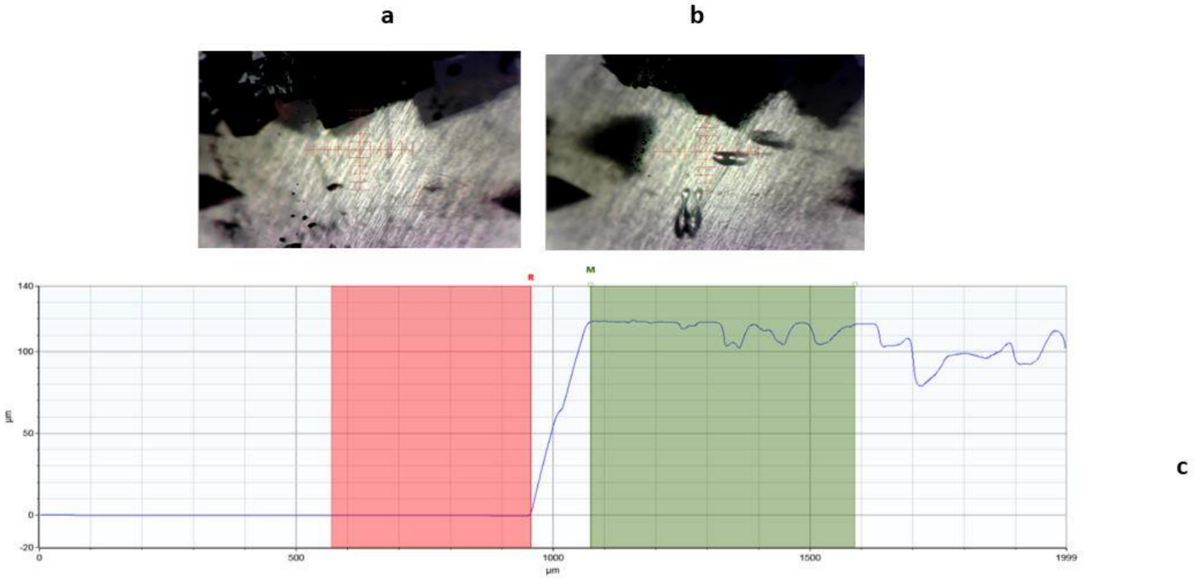

Figure 17. Bruker Dektak-XT Stylus Surface Profiling System results for the thickness of MAPbBr$_3$ crystalline thin film a) first location b) second location c) plot legend of MAPbBr$_3$ single-crystalline thin film thickness

For measurement, the scan type was selected as standard. Hills and valleys were selected with a radius of 125 μm and length of 2000 μm for 10 secs, and a resolution of 0.66 (μm/pt), and speed of 200 μm/sec were set up.

Chap 3. Conclusion and Outlook

3.1 Summary of the LHP halide exchange experiments

Using ILs (BMIMI, and/or BMIMCl) for the halide diffusion and transport in the single crystalline LHP thin film with a thickness, ranging from 100-800 µm has been attempted. PL and SEM-EDX were attempted to demonstrate halide gradient over multi-micron length scales. The results from both methods showed the absence of a halide gradient.

3.2 Future Outlook

3.2.1 Fast halide exchange of Cl/Br co-insertion into the perovskite lattice thin films at room temperature

In this work, halide exchange in LHPs with a general formula of $MAPbX_3$ (X: Cl, Br, or I) was attempted. In brief, at ambient temperature, the halide substitution in the $MAPbBr_3$ single-crystalline thin films followed by a hydrophobic treatment of the substrate is rapid and experiences different phases within minutes or less than an hour after contact with the precursor solutions of $MAPbCl_3$. However, exceptions were also visualized for bromide conversation by iodide at room temperature on the $MAPbBr_3$ single-crystalline thin films. In addition to this, using $MAPbBr_3$ single-crystalline thin films without hydrophobic treatment of the substrate demonstrated a color change on the surface at ambient temperature. However, no further new reactions or crystallization was seen on the surface of $MAPbBr_3$ single-crystalline thin films. For further studies, solid-state NMR, as a non-destructive strategy along with a controllable anion exchange of halide perovskite films, photoluminescence (PL) mapping, Low-Frequency Raman, XPS, and SEM combined with EDX are proposed to investigate the reactions, crystal structures, rate of halide diffusion, and Pb environment.

References

1. Jena, A.K., A. Kulkarni, and T. Miyasaka, *Halide Perovskite Photovoltaics: Background, Status, and Future Prospects.* Chemical Reviews, 2019. **119**(5): p. 3036-3103.
2. Akkerman, Q.A. and L. Manna, *What Defines a Halide Perovskite?* ACS Energy Letters, 2020. **5**(2): p. 604-610.
3. Dong, Q., et al., *Solar cells. Electron-hole diffusion lengths > 175 μm in solution-grown CH3NH3PbI3 single crystals.* Science, 2015. **347**(6225): p. 967-70.
4. Chilvery, A., et al., *A perspective on the recent progress in solution-processed methods for highly efficient perovskite solar cells.* Science and technology of advanced materials, 2016. **17**(1): p. 650-658.
5. Shamsi, J., et al., *Metal Halide Perovskite Nanocrystals: Synthesis, Post-Synthesis Modifications, and Their Optical Properties.* Chemical Reviews, 2019. **119**(5): p. 3296-3348.
6. Johnsson, M. and P. Lemmens, *Crystallography and Chemistry of Perovskites*, in *Handbook of Magnetism and Advanced Magnetic Materials*. 2007.
7. Zhao, Y. and K. Zhu, *Organic-inorganic hybrid lead halide perovskites for optoelectronic and electronic applications.* Chemical Society Reviews, 2016. **45**(3): p. 655-689.
8. Kim, H.-S., et al., *Lead Iodide Perovskite Sensitized All-Solid-State Submicron Thin Film Mesoscopic Solar Cell with Efficiency Exceeding 9%.* Scientific Reports, 2012. **2**(1): p. 591.

9. Yang, Z., A. Rajagopal, and A.K.-Y. Jen, *Ideal Bandgap Organic-Inorganic Hybrid Perovskite Solar Cells.* Advanced Materials, 2017. **29**(47): p. 1704418.

10. Zhang, Z., et al., *Tunability of Band Gap and Photoluminescence in CH3NH3PbI3 Films by Anodized Aluminum Oxide Templates.* Scientific Reports, 2017. **7**(1): p. 1918.

11. Wang, Y., et al., *High-Efficiency Flexible Solar Cells Based on Organometal Halide Perovskites.* Adv Mater, 2016. **28**(22): p. 4532-40.

12. Keivanidis, P.E., et al., *X-ray stability and the response of polymeric photodiodes for imaging applications.* Applied Physics Letters, 2008. **92**(2): p. 023304.

13. Gill, H.S., et al., *Flexible perovskite-based X-ray detectors for dose monitoring in medical imaging applications.* Physics in Medicine, 2018. **5**: p. 20-23.

14. Boroumand, F.A., et al., *Direct x-ray detection with conjugated polymer devices.* Applied Physics Letters, 2007. **91**(3): p. 033509.

15. Satapathi, S., et al., *Synthesis of nanoparticles of P3HT and PCBM for optimizing morphology in polymeric solar cells.* Applied Surface Science, 2014. **323**: p. 13-18.

16. Stavrakas, C., et al., *Visualizing Buried Local Carrier Diffusion in Halide Perovskite Crystals via Two-Photon Microscopy.* ACS energy letters, 2020. **5**(1): p. 117-123.

17. Nocera, D.G., *Personalized Energy: The Home as a Solar Power Station and Solar Gas Station.* ChemSusChem, 2009. **2**(5): p. 387-390.

18. Kojima, A., et al., *Organometal halide perovskites as visible-light sensitizers for photovoltaic cells.* J Am Chem Soc, 2009. **131**(17): p. 6050-1.

19. Kim, Y.-H., et al., *Multicolored Organic/Inorganic Hybrid Perovskite Light-Emitting Diodes.* Advanced Materials, 2015. **27**(7): p. 1248-1254.

20. Dirin, D.N., et al., *Harnessing Defect-Tolerance at the Nanoscale: Highly Luminescent Lead Halide Perovskite Nanocrystals in Mesoporous Silica Matrixes.* Nano Letters, 2016. **16**(9): p. 5866-5874.

21. Veldhuis, S.A., et al., *Perovskite Materials for Light-Emitting Diodes and Lasers.* Adv Mater, 2016. **28**(32): p. 6804-34.

22. Le, Q.V., et al., *Structural Investigation of Cesium Lead Halide Perovskites for High-Efficiency Quantum Dot Light-Emitting Diodes.* The Journal of Physical Chemistry Letters, 2017. **8**(17): p. 4140-4147.

23. Hong, K., et al., *Low-dimensional halide perovskites: review and issues.* Journal of Materials Chemistry C, 2018. **6**(9): p. 2189-2209.

24. Hu, X., et al., *High-Performance Flexible Broadband Photodetector Based on Organolead Halide Perovskite.* Advanced Functional Materials, 2014. **24**(46): p. 7373-7380.

25. Dong, R., et al., *High-gain and low-driving-voltage photodetectors based on organolead triiodide perovskites.* Adv Mater, 2015. **27**(11): p. 1912-8.

26. Fang, Y. and J. Huang, *Resolving Weak Light of Sub-picowatt per Square Centimeter by Hybrid Perovskite Photodetectors Enabled by Noise Reduction.* Advanced Materials, 2015. **27**(17): p. 2804-2810.

27. Kwon, K.C., et al., *Inhibition of Ion Migration for Reliable Operation of Organolead Halide Perovskite-Based Metal/Semiconductor/Metal Broadband Photodetectors.* Advanced Functional Materials, 2016. **26**(23): p. 4213-4222.

28. Eaton, S.W., et al., *Lasing in robust cesium lead halide perovskite nanowires.* Proceedings of the National Academy of Sciences of the United States of America, 2016. **113**(8): p. 1993-1998.

29. Liu, P., et al., *Organic-Inorganic Hybrid Perovskite Nanowire Laser Arrays.* ACS Nano, 2017. **11**(6): p. 5766-5773.

30. Xing, J., et al., *Vapor Phase Synthesis of Organometal Halide Perovskite Nanowires for Tunable Room-Temperature Nanolasers.* Nano Letters, 2015. **15**(7): p. 4571-4577.

31. Fu, Y., et al., *Broad Wavelength Tunable Robust Lasing from Single-Crystal Nanowires of Cesium Lead Halide Perovskites (CsPbX3, X = Cl, Br, I).* ACS Nano, 2016. **10**(8): p. 7963-72.

32. Choi, J., et al., *Organolead Halide Perovskites for Low Operating Voltage Multilevel Resistive Switching.* Adv Mater, 2016. **28**(31): p. 6562-7.

33. Choi, J., et al., *Enhanced Endurance Organolead Halide Perovskite Resistive Switching Memories Operable under an Extremely Low Bending Radius.* ACS Appl Mater Interfaces, 2017. **9**(36): p. 30764-30771.

34. Gu, C. and J.-S. Lee, *Flexible Hybrid Organic–Inorganic Perovskite Memory.* ACS Nano, 2016. **10**(5): p. 5413-5418.

35. Chin, X.Y., et al., *Lead iodide perovskite light-emitting field-effect transistor.* Nature Communications, 2015. **6**(1): p. 7383.

36. Yoo, E.J., et al., *Resistive Switching Behavior in Organic–Inorganic Hybrid CH3NH3PbI3−xClx Perovskite for Resistive Random Access Memory Devices.* Advanced Materials, 2015. **27**(40): p. 6170-6175.

37. Cuhadar, C., et al., *All-Inorganic Bismuth Halide Perovskite-Like Materials A3Bi2I9 and A3Bi1.8Na0.2I8.6 (A = Rb and Cs) for Low-Voltage Switching Resistive Memory.* ACS Applied Materials & Interfaces, 2018. **10**(35): p. 29741-29749.

38. Zhang, S., et al., *Resistive switching characteristics of MnOx-based ReRAM.* Journal of Physics D: Applied Physics, 2009. **42**(5): p. 055112.

39. Natali, D. and M. Sampietro, *Detectors based on organic materials: status and perspectives.* Nuclear Instruments and Methods in Physics Research Section A: Accelerators, Spectrometers, Detectors and Associated Equipment, 2003. **512**(1): p. 419-426.

40. Agostinelli, T., et al., *A polymer/fullerene-based photodetector with the extremely low dark current for x-ray medical imaging applications.* Applied Physics Letters, 2008. **93**(20): p. 203305.

41. Ng, T.N., et al., *Flexible image sensor array with bulk heterojunction organic photodiode.* Applied Physics Letters, 2008. **92**(21): p. 213303.

42. Kingsley, J.W., et al., *Detecting 6MV X-rays using an organic photovoltaic device.* Organic Electronics, 2009. **10**(6): p. 1170-1173.

43. Mills, C.A., et al., *Enhanced x-ray detection sensitivity in semiconducting polymer diodes containing metallic nanoparticles.* Journal of Physics D: Applied Physics, 2013. **46**(27): p. 275102.

44. Intaniwet, A., et al., *Achieving a Stable Time Response in Polymeric Radiation Sensors under Charge Injection by X-rays.* ACS Applied Materials & Interfaces, 2010. **2**(6): p. 1692-1699.

45. Arca, F., et al., *Interface trap states in organic photodiodes.* Scientific reports, 2013. **3**: p. 1324.

46. Hao, F., et al., *Lead-free solid-state organic-inorganic halide perovskite solar cells.* Nature Photonics, 2014. **8**(6): p. 489-494.

47. Li, M., et al., *Pressure responses of halide perovskites with various compositions, dimensionalities, and morphologies.* Matter and Radiation at Extremes, 2020. **5**(1): p. 018201.

48. Miyasaka, T., *Lead Halide Perovskites in Thin Film Photovoltaics: Background and Perspectives.* Bulletin of the Chemical Society of Japan, 2018. **91**(7): p. 1058-1068.

49. Cho, H., et al., *Overcoming the electroluminescence efficiency limitations of perovskite light-emitting diodes.* Science, 2015. **350**(6265): p. 1222-5.

50. Wang, W., et al., *High-performance perovskite light-emitting diodes based on double hole transport layers.* Journal of Materials Chemistry C, 2021. **9**(6): p. 2115-2122.

51. Paulo-Mirasol, S., E. Martínez-Ferrero, and E. Palomares, *Direct white light emission from carbon nanodots (C-dots) in solution processed light emitting diodes.* Nanoscale, 2019. **11**(23): p. 11315-11321.

52. Ou, Q., et al., *Band structure engineering in metal halide perovskite nanostructures for optoelectronic applications.* Nano Materials Science, 2019. **1**(4): p. 268-287.

53. Yakunin, S., et al., *Non-dissipative internal optical filtering with solution-grown perovskite single crystals for full-colour imaging.* NPG Asia Materials, 2017. **9**(9): p. e431-e431.

54. Yakunin, S., et al., *Detection of X-ray photons by solution-processed organic-inorganic perovskites.* Nature photonics, 2015. **9**(7): p. 444-449.

55. Wei, W., et al., *Monolithic integration of hybrid perovskite single crystals with heterogenous substrate for highly sensitive X-ray imaging.* Nature Photonics, 2017. **11**(5): p. 315-321.

56. Kim, Y.C., et al., *Printable organometallic perovskite enables large-area, low-dose X-ray imaging.* Nature, 2017. **550**(7674): p. 87-91.

57. Sum, T.C. and N. Mathews, *Advancements in perovskite solar cells: photophysics behind the photovoltaics.* Energy & Environmental Science, 2014. **7**(8): p. 2518-2534.

58. Kim, J., et al., *The Role of Intrinsic Defects in Methylammonium Lead Iodide Perovskite.* J Phys Chem Lett, 2014. **5**(8): p. 1312-7.

59. Miyano, K., et al., *Lead Halide Perovskite Photovoltaic as a Model p–i–n Diode.* Accounts of Chemical Research, 2016. **49**(2): p. 303-310.

60. Tanaka, K., et al., *Comparative study on the excitons in lead-halide-based perovskite-type crystals CH3NH3PbBr3 CH3NH3PbI3.* Solid State Communications, 2003. **127**(9): p. 619-623.

61. Yin, W.-J., T. Shi, and Y. Yan, *Superior Photovoltaic Properties of Lead Halide Perovskites: Insights from First-Principles Theory.* The Journal of Physical Chemistry C, 2015. **119**(10): p. 5253-5264.

62. Green, M.A., A. Ho-Baillie, and H.J. Snaith, *The emergence of perovskite solar cells.* Nature Photonics, 2014. **8**(7): p. 506-514.

63. Stranks, S.D., et al., *Electron-Hole Diffusion Lengths Exceeding 1 Micrometer in an Organometal Trihalide Perovskite Absorber.* Science, 2013. **342**(6156): p. 341-344.

64. Ishi, J., et al., *Third-Order Optical Nonlinearity Due to Excitons and Biexcitons in a Self-Organized Quantum-Well Material (C6H13NH3)2PbI4.* Journal of Nonlinear Optical Physics & Materials, 1998. **07**(01): p. 153-159.

65. Giorgi, G., et al., *Small Photocarrier Effective Masses Featuring Ambipolar Transport in Methylammonium Lead Iodide Perovskite: A Density Functional Analysis.* The Journal of Physical Chemistry Letters, 2013. **4**(24): p. 4213-4216.

66. Wells, H.L., *On the rubidium-lead halides, and a summary of the double halides of lead.* American Journal of Science, 1893. **s3-46**(271): p. 34-38.

67. Ema, K., et al., *Huge exchange energy and fine structure of excitons in an organic-inorganic quantum well material.* Physical Review B, 2006. **73**(24): p. 241310.

68. Stranks, S.D. and H.J. Snaith, *Metal-halide perovskites for photovoltaic and light-emitting devices.* Nature Nanotechnology, 2015. **10**(5): p. 391-402.

69. Kim, Y.H., et al., *Multicolored organic/inorganic hybrid perovskite light-emitting diodes.* Adv Mater, 2015. **27**(7): p. 1248-54.

70. Muratov, D.S., et al., *Slot-Die-Printed Two-Dimensional ZrS3 Charge Transport Layer for Perovskite Light-Emitting Diodes.* ACS Applied Materials & Interfaces, 2019. **11**(51): p. 48021-48028.

71. Kasap, S., et al., *Amorphous and Polycrystalline Photoconductors for Direct Conversion Flat Panel X-Ray Image Sensors.* Sensors, 2011. **11**(5): p. 5112-5157.

72. Oh, K.M., et al., *Measurement of the electrical properties of a polycrystalline cadmium telluride for direct conversion flat panel x-ray detector.* Journal of Instrumentation, 2014. **9**(01): p. P01010-P01010.

73. Kasap, S.O. and J.A. Rowlands, *Review X-ray photoconductors and stabilized a-Se for direct conversion digital flat-panel X-ray image-detectors.* Journal of Materials Science: Materials in Electronics, 2000. **11**(3): p. 179-198.

74. Eijk, C.W.E.v., *Inorganic scintillators in medical imaging.* Physics in Medicine and Biology, 2002. **47**(8): p. R85-R106.

75. !!! INVALID CITATION !!! [80, 85].

76. Jr., N.H. and S.F. Bevacqua, *COHERENT (VISIBLE) LIGHT EMISSION FROM Ga(As1−xPx) JUNCTIONS.* Applied Physics Letters, 1962. **1**(4): p. 82-83.

77. Hall, R.N., et al., *Coherent Light Emission From GaAs Junctions.* Physical Review Letters, 1962. **9**(9): p. 366-368.

78. Amano, H., et al., *Metalorganic vapor phase epitaxial growth of a high quality GaN film using an AlN buffer layer*. Applied Physics Letters, 1986. **48**(5): p. 353-355.

79. Höfler, G.E., et al. *High-flux, high-efficiency transparent-substrate AlGaInP/GaP light-emitting diodes*. Electronics Letters, 1998. **34**, 1781-1782.

80. Krames, M.R., et al., *Status and Future of High-Power Light-Emitting Diodes for Solid-State Lighting.* Journal of Display Technology, 2007. **3**(2): p. 160-175.

81. Maruska, H.P. and W.C. Rhines, *A modern perspective on the history of semiconductor nitride blue light sources.* Solid-State Electronics, 2015. **111**: p. 32-41.

82. Tang, C.W. and S.A. VanSlyke, *Organic electroluminescent diodes.* Applied Physics Letters, 1987. **51**(12): p. 913-915.

83. Bellmann, E., et al., *New Triarylamine-Containing Polymers as Hole Transport Materials in Organic Light-Emitting Diodes: Effect of Polymer Structure and Cross-Linking on Device Characteristics.* Chemistry of Materials, 1998. **10**(6): p. 1668-1676.

84. Hebner, T.R., et al., *Ink-jet printing of doped polymers for organic light emitting devices.* Applied Physics Letters, 1998. **72**(5): p. 519-521.

85. Duarte, F.J., L.S. Liao, and K.M. Vaeth, *Coherence characteristics of electrically excited tandem organic light-emitting diodes.* Optics Letters, 2005. **30**(22): p. 3072-3074.

86. Burroughes, J.H., et al., *Light-emitting diodes based on conjugated polymers.* Nature, 1990. **347**(6293): p. 539-541.

87. Bharathan, J. and Y. Yang, *Polymer electroluminescent devices processed by inkjet printing: I. Polymer light-emitting logo.* Applied Physics Letters, 1998. **72**(21): p. 2660-2662.

88. Ki Bae, W., et al., *Deep blue light-emitting diodes based on Cd1−xZnxS@ZnS quantum dots.* Nanotechnology, 2009. **20**(7): p. 075202.

89. Bae, W.K., et al., *Multicolored Light-Emitting Diodes Based on All-Quantum-Dot Multilayer Films Using Layer-by-Layer Assembly Method.* Nano Letters, 2010. **10**(7): p. 2368-2373.

90. Bae, W.K., et al., *Highly Efficient Green-Light-Emitting Diodes Based on CdSe@ZnS Quantum Dots with a Chemical-Composition Gradient.* Advanced Materials, 2009. **21**(17): p. 1690-1694.

91. Shirasaki, Y., et al., *Emergence of colloidal quantum-dot light-emitting technologies.* Nature Photonics, 2013. **7**(1): p. 13-23.

92. Dai, X., et al., *Solution-processed, high-performance light-emitting diodes based on quantum dots.* Nature, 2014. **515**(7525): p. 96-99.

93. Mashford, B.S., et al., *High-efficiency quantum-dot light-emitting devices with enhanced charge injection.* Nature Photonics, 2013. **7**(5): p. 407-412.

94. Xing, G., et al., *Low-temperature solution-processed wavelength-tunable perovskites for lasing.* Nature Materials, 2014. **13**(5): p. 476-480.

95. Wang, J., et al., *Interfacial Control Toward Efficient and Low-Voltage Perovskite Light-Emitting Diodes.* Advanced Materials, 2015. **27**(14): p. 2311-2316.

96. Cho, H., et al., *Overcoming the electroluminescence efficiency limitations of perovskite light-emitting diodes.* Science, 2015. **350**(6265): p. 1222-1225.

97. Sadhanala, A., et al., *Blue-Green Color Tunable Solution Processable Organolead Chloride–Bromide Mixed Halide Perovskites for Optoelectronic Applications.* Nano Letters, 2015. **15**(9): p. 6095-6101.

98. Jaramillo-Quintero, O.A., et al., *Bright Visible-Infrared Light Emitting Diodes Based on Hybrid Halide Perovskite with Spiro-OMeTAD as a Hole-Injecting Layer.* The Journal of Physical Chemistry Letters, 2015. **6**(10): p. 1883-1890.

99. Pathak, S., et al., *Perovskite Crystals for Tunable White Light Emission.* Chemistry of Materials, 2015. **27**(23): p. 8066-8075.

100. Hoye, R.L.Z., et al., *Enhanced Performance in Fluorene-Free Organometal Halide Perovskite Light-Emitting Diodes using Tunable, Low Electron Affinity Oxide Electron Injectors.* Advanced Materials, 2015. **27**(8): p. 1414-1419.

101. Tan, Z.-K., et al., *Bright light-emitting diodes based on organometal halide perovskite.* Nature Nanotechnology, 2014. **9**(9): p. 687-692.

102. Byun, J., et al., *Efficient Visible Quasi-2D Perovskite Light-Emitting Diodes.* Advanced Materials, 2016. **28**(34): p. 7515-7520.

103. Li, J., et al., *Single-Layer Light-Emitting Diodes Using Organometal Halide Perovskite/Poly(ethylene oxide) Composite Thin Films.* Advanced Materials, 2015. **27**(35): p. 5196-5202.

104. Li, J., et al., *Giant Enhancement of Internal Electric Field Boosting Bulk Charge Separation for Photocatalysis.* Advanced Materials, 2016. **28**(21): p. 4059-4064.

105. Watthage, S.C., et al., *Chapter 3 - Evolution of Perovskite Solar Cells*, in *Perovskite Photovoltaics*, S. Thomas and A. Thankappan, Editors. 2018, Academic Press. p. 43-88.

106. Wang, J., et al., *Halide perovskite based on hydrophobic ionic liquid for stability improving and its application in high-efficient photovoltaic cell.* Electrochimica Acta, 2019. **303**: p. 133-139.

107. Lewis, N.S., *Powering the Planet.* MRS Bulletin, 2011. **32**(10): p. 808-820.

108. Xia, C.Q., et al., *Limits to Electrical Mobility in Lead-Halide Perovskite Semiconductors.* The Journal of Physical Chemistry Letters, 2021. **12**(14): p. 3607-3617.

109. Burschka, J., et al., *Sequential deposition as a route to high-performance perovskite-sensitized solar cells.* Nature, 2013. **499**(7458): p. 316-319.

110. Jeon, N.J., et al., *Solvent engineering for high-performance inorganic-organic hybrid perovskite solar cells.* Nat Mater, 2014. **13**(9): p. 897-903.

111. Xiao, M., et al., *A Fast Deposition-Crystallization Procedure for Highly Efficient Lead Iodide Perovskite Thin-Film Solar Cells.* Angewandte Chemie International Edition, 2014. **53**(37): p. 9898-9903.

112. Nie, W., et al., *Solar cells. High-efficiency solution-processed perovskite solar cells with millimeter-scale grains.* Science, 2015. **347**(6221): p. 522-5.

113. Ding, J., et al., *Fully Air-Bladed High-Efficiency Perovskite Photovoltaics.* Joule, 2019. **3**(2): p. 402-416.

114. Yin, J., et al., *Vapor-assisted crystallization control toward high performance perovskite photovoltaics with over 18% efficiency in the ambient atmosphere.* Journal of Materials Chemistry A, 2016. **4**(34): p. 13203-13210.

115. Fan, P., et al., *High-performance perovskite CH3NH3PbI3 thin films for solar cells prepared by single-source physical vapour deposition.* Sci Rep, 2016. **6**: p. 29910.

116. Hsiao, S.Y., et al., *Efficient All-Vacuum Deposited Perovskite Solar Cells by Controlling Reagent Partial Pressure in High Vacuum.* Adv Mater, 2016. **28**(32): p. 7013-9.

117. Momblona, C., et al., *Efficient vacuum deposited p-i-n and n-i-p perovskite solar cells employing doped charge transport layers.* Energy & Environmental Science, 2016. **9**(11): p. 3456-3463.

118. Herz, L.M., *Charge-Carrier Mobilities in Metal Halide Perovskites: Fundamental Mechanisms and Limits.* ACS Energy Letters, 2017. **2**(7): p. 1539-1548.

119. Wehrenfennig, C., et al., *Charge-carrier dynamics in vapour-deposited films of the organolead halide perovskite CH3NH3PbI3−xClx.* Energy & Environmental Science, 2014. **7**(7): p. 2269-2275.

120. Wehrenfennig, C., et al., *High charge carrier mobilities and lifetimes in organolead trihalide perovskites.* Adv Mater, 2014. **26**(10): p. 1584-9.

121. Milot, R.L., et al., *Temperature-Dependent Charge-Carrier Dynamics in CH3NH3PbI3 Perovskite Thin Films.* Advanced Functional Materials, 2015. **25**(39): p. 6218-6227.

122. Shi, D., et al., *Solar cells. Low trap-state density and long carrier diffusion in organolead trihalide perovskite single crystals.* Science, 2015. **347**(6221): p. 519-22.

123. Valverde-Chávez, D.A., et al., *Intrinsic femtosecond charge generation dynamics in single crystal CH3NH3PbI3.* Energy & Environmental Science, 2015. **8**(12): p. 3700-3707.

124. Chen, T., et al., *Origin of long lifetime of band-edge charge carriers in organic–inorganic lead iodide perovskites.* Proceedings of the National Academy of Sciences, 2017. **114**(29): p. 7519-7524.

125. Hutter, E.M., et al., *Direct-indirect character of the bandgap in methylammonium lead iodide perovskite.* Nat Mater, 2017. **16**(1): p. 115-120.

126. Zheng, F., et al., *Rashba Spin-Orbit Coupling Enhanced Carrier Lifetime in* $CH_3NH_3PbI_3$*.* Nano Lett, 2015. **15**(12): p. 7794-800.

127. Chen, Y., et al., *Extended carrier lifetimes and diffusion in hybrid perovskites revealed by Hall effect and photoconductivity measurements.* Nature Communications, 2016. **7**(1): p. 12253.

128. Pazos-Outón, L.M., et al., *Photon recycling in lead iodide perovskite solar cells.* Science, 2016. **351**(6280): p. 1430-3.

129. Zhu, H., et al., *Screening in crystalline liquids protects energetic carriers in hybrid perovskites.* Science, 2016. **353**(6306): p. 1409-1413.

130. Zhu, X.Y. and V. Podzorov, *Charge Carriers in Hybrid Organic–Inorganic Lead Halide Perovskites Might Be Protected as Large Polarons.* The Journal of Physical Chemistry Letters, 2015. **6**(23): p. 4758-4761.

131. Frost, J.M., et al., *Atomistic Origins of High-Performance in Hybrid Halide Perovskite Solar Cells.* Nano Letters, 2014. **14**(5): p. 2584-2590.

132. Frost, J.M., K.T. Butler, and A. Walsh, *Molecular ferroelectric contributions to anomalous hysteresis in hybrid perovskite solar cells.* APL Materials, 2014. **2**(8): p. 081506.

133. Kutes, Y., et al., *Direct Observation of Ferroelectric Domains in Solution-Processed CH3NH3PbI3 Perovskite Thin Films.* The Journal of Physical Chemistry Letters, 2014. **5**(19): p. 3335-3339.

134. Liu, S., et al., *Ferroelectric Domain Wall Induced Band Gap Reduction and Charge Separation in Organometal Halide Perovskites.* The Journal of Physical Chemistry Letters, 2015. **6**(4): p. 693-699.

135. Etienne, T., E. Mosconi, and F. De Angelis, *Dynamical Origin of the Rashba Effect in Organohalide Lead Perovskites: A Key to Suppressed Carrier Recombination in Perovskite Solar Cells?* The Journal of Physical Chemistry Letters, 2016. **7**(9): p. 1638-1645.

136. Johnston, M.B. and L.M. Herz, *Hybrid Perovskites for Photovoltaics: Charge-Carrier Recombination, Diffusion, and Radiative Efficiencies.* Accounts of Chemical Research, 2016. **49**(1): p. 146-154.

137. Xing, G., et al., *Long-Range Balanced Electron- and Hole-Transport Lengths in Organic-Inorganic CH₃NH₃PbI₃.* Science, 2013. **342**(6156): p. 344-347.

138. Ball, J.M. and A. Petrozza, *Defects in perovskite-halides and their effects in solar cells.* Nature Energy, 2016. **1**(11): p. 16149.

139. Tao, S.X., X. Cao, and P.A. Bobbert, *Accurate and efficient band gap predictions of metal halide perovskites using the DFT-1/2 method: GW accuracy with DFT expense.* Scientific Reports, 2017. **7**(1): p. 14386.

140. Ko, Y., et al., *Microtuning of the Wide-Bandgap Perovskite Lattice Plane for Efficient and Robust High-Voltage Planar Solar Cells Exceeding 1.5 V.* ACS Applied Energy Materials, 2020. **3**(3): p. 2331-2341.

141. Comparotto, C., et al., *Chalcogenide Perovskite BaZrS3: Thin Film Growth by Sputtering and Rapid Thermal Processing.* ACS Applied Energy Materials, 2020. **3**(3): p. 2762-2770.

142. Redondo-Obispo, C., et al., *Enhanced Nonlinear Optical Coefficients of MAPbI3 Thin Films by Bismuth Doping.* The Journal of Physical Chemistry Letters, 2020. **11**(6): p. 2188-2194.

143. Dehnhardt, N., et al., *Multinary Halogenido Bismuthates beyond the Double Perovskite Motif.* Inorganic Chemistry, 2020. **59**(6): p. 3394-3405.

144. Vickers, E.T., et al., *Enhancing Charge Carrier Delocalization in Perovskite Quantum Dot Solids with Energetically Aligned Conjugated Capping Ligands.* ACS Energy Letters, 2020. **5**(3): p. 817-825.

145. Zhang, H.-Y., et al., *A Three-Dimensional Lead Halide Perovskite-Related Ferroelectric.* Journal of the American Chemical Society, 2020. **142**(10): p. 4604-4608.

146. Rybin, N., et al., *Effects of Chlorine Mixing on Optoelectronics, Ion Migration, and Gamma-Ray Detection in Bromide Perovskites.* Chemistry of Materials, 2020. **32**(5): p. 1854-1863.

147. Beimborn, J.C., et al., *Size-Dependent Pressure-Response of the Photoluminescence of CsPbBr3 Nanocrystals.* The Journal of Physical Chemistry Letters, 2020. **11**(5): p. 1975-1980.

148. Cui, Y., et al., *Correlating Hysteresis and Stability with Organic Cation Composition in the Two-Step Solution-Processed Perovskite Solar Cells.* ACS Applied Materials & Interfaces, 2020. **12**(9): p. 10588-10596.

149. Wang, D., et al., *Highly Efficient CsPbBr3 Planar Perovskite Solar Cells via Additive Engineering with NH4SCN.* ACS Applied Materials & Interfaces, 2020. **12**(9): p. 10579-10587.

150. Chavan, R.D., et al., *Atomic Layer Deposition of an Effective Interface Layer of TiN for Efficient and Hysteresis-Free Mesoscopic Perovskite Solar Cells.* ACS Applied Materials & Interfaces, 2020. **12**(7): p. 8098-8106.

151. Li, T., et al., *Origin of Broad-Band Emission and Impact of Structural Dimensionality in Tin-Alloyed Ruddlesden–Popper Hybrid Lead Iodide Perovskites.* ACS Energy Letters, 2020. **5**(2): p. 347-352.

152. Sekimoto, T., et al., *Inverse Temperature Crystallization of Formamidinium Tin Iodide: Indirect Transition State and Restriction of Cation Motion.* Crystal Growth & Design, 2020. **20**(2): p. 874-883.

153. Li, J., et al., *Biological impact of lead from halide perovskites reveals the risk of introducing a safe threshold.* Nature Communications, 2020. **11**(1): p. 310.

154. Lanzetta, L., N. Aristidou, and S.A. Haque, *Stability of Lead and Tin Halide Perovskites: The Link between Defects and Degradation.* The Journal of Physical Chemistry Letters, 2020. **11**(2): p. 574-585.

155. Nishida, J., et al., *Heterogeneous Cation–Lattice Interaction and Dynamics in Triple-Cation Perovskites Revealed by Infrared Vibrational Nanoscopy.* ACS Energy Letters, 2020. **5**(5): p. 1636-1643.

156. Ng, T.K., et al., *Group-III-nitride and halide-perovskite semiconductor gain media for amplified spontaneous emission and lasing applications.* Journal of Physics D: Applied Physics, 2021. **54**(14): p. 143001.

157. Li, D., et al., *Chiral Lead-Free Hybrid Perovskites for Self-Powered Circularly Polarized Light Detection.* Angewandte Chemie International Edition, 2021. **60**(15): p. 8415-8418.

158. Piper, R.T., et al., *Photonic Curing of Nickel Oxide Transport Layer and Perovskite Active Layer for Flexible Perovskite Solar Cells: A Path Towards High-Throughput Manufacturing.* Frontiers in Energy Research, 2021. **9**(76).

159. Leupold, N. and F. Panzer, *Recent Advances and Perspectives on Powder-Based Halide Perovskite Film Processing.* Advanced Functional Materials, 2021. **31**(14): p. 2007350.

160. Yang, C.-M. and F.-C. Chen, *Position Effects of Metal Nanoparticles on the Performance of Perovskite Light-Emitting Diodes.* Nanomaterials, 2021. **11**(4): p. 993.

161. Zhao, J., et al., *Photo-Diodes Based on CH3NH3PbCl3 Perovskite Single Crystals by Epitaxial Growth for Ultraviolet Photo-Detection.* Frontiers in Physics, 2021. **9**(129).

162. Brenner, T.M., et al., *Hybrid organic—inorganic perovskites: low-cost semiconductors with intriguing charge-transport properties.* Nature Reviews Materials, 2016. **1**(1): p. 15007.

163. Osherov, A., et al., *Halide Diffusion in MAPbX3: Limits to Topotaxy for Halide Exchange in Perovskites.* Chemistry of Materials, 2020. **32**(10): p. 4223-4231.

164. Bhalla, A.S., R. Guo, and R. Roy, *The perovskite structure—a review of its role in ceramic science and technology.* Materials Research Innovations, 2000. **4**(1): p. 3-26.

165. Jiang, H., et al., *Ion exchange for halide perovskite: From nanocrystal to bulk materials.* Nano Select. **n/a**(n/a).

166. Kamat, P.V. and M. Kuno, *Halide Ion Migration in Perovskite Nanocrystals and Nanostructures.* Acc Chem Res, 2021. **54**(3): p. 520-531.

167. Li, G., et al., *Reversible Anion Exchange Reaction in Solid Halide Perovskites and Its Implication in Photovoltaics.* The Journal of Physical Chemistry C, 2015. **119**(48): p. 26883-26888.

168. Lai, M., et al., *Intrinsic anion diffusivity in lead halide perovskites is facilitated by a soft lattice.* Proceedings of the National Academy of Sciences, 2018. **115**(47): p. 11929-11934.

169. Luo, Y., et al., *Spatially Heterogeneous Chlorine Incorporation in Organic–Inorganic Perovskite Solar Cells.* Chemistry of Materials, 2016. **28**(18): p. 6536-6543.

170. Zhao, Y., et al., *Effects of ion migration and improvement strategies for the operational stability of perovskite solar cells.* Physical Chemistry Chemical Physics, 2021. **23**(1): p. 94-106.

171. Yuan, Y. and J. Huang, *Ion Migration in Organometal Trihalide Perovskite and Its Impact on Photovoltaic Efficiency and Stability.* Accounts of Chemical Research, 2016. **49**(2): p. 286-293.

172. Simon, P. and Y. Gogotsi, *Materials for electrochemical capacitors.* Nat Mater, 2008. **7**(11): p. 845-54.

173. Li, H., et al., *Photoferroelectric perovskite solar cells: Principles, advances and insights.* Nano Today, 2021. **37**: p. 101062.

174. Li, W., et al., *Plasmonic metasurface for light absorption enhancement in GaAs thin film.* Plasmonics, 2016. **11**(5): p. 1401-1406.

175. Senocrate, A. and J. Maier, *Solid-State Ionics of Hybrid Halide Perovskites.* Journal of the American Chemical Society, 2019. **141**(21): p. 8382-8396.

176. Ceratti, D.R., et al., *Self-Healing Inside APbBr3 Halide Perovskite Crystals.* Advanced Materials, 2018. **30**(10): p. 1706273.

177. Ceratti, D.R., et al., *The pursuit of stability in halide perovskites: the monovalent cation and the key for surface and bulk self-healing.* Materials Horizons, 2021. **8**(5): p. 1570-1586.

178. Shrotriya, V., et al., *Accurate Measurement and Characterization of Organic Solar Cells.* Advanced Functional Materials, 2006. **16**(15): p. 2016-2023.

179. Adhyaksa, G.W.P., et al., *Understanding Detrimental and Beneficial Grain Boundary Effects in Halide Perovskites.* Advanced Materials, 2018. **30**(52): p. 1804792.

180. Khassaf, H., et al., *Effect of Grain Boundaries on Charge Transport in Methylammonium Lead Iodide Perovskite Thin Films.* The Journal of Physical Chemistry C, 2019. **123**(9): p. 5321-5325.

181. Zhang, Y., et al., *Quantitative imaging of anion exchange kinetics in halide perovskites.* Proceedings of the National Academy of Sciences, 2019. **116**(26): p. 12648-12653.

182. Efrati, A., et al., *First evidence of macroscale single crystal ion exchange found in lead halide perovskites.* EcoMat, 2020. **2**(1): p. e12016.

183. Walsh, A., et al., *Self-regulation mechanism for charged point defects in hybrid halide perovskites.* Angewandte Chemie (International ed. in English), 2015. **54**(6): p. 1791-1794.

184. Jacobs, M.H., *Diffusion Processes*, in *Diffusion Processes*. 1935, Springer Berlin Heidelberg: Berlin, Heidelberg. p. 1-145.

185. Durand-Charre, M., *Diffusion*, in *Microstructure of Steels and Cast Irons*. 2004, Springer Berlin Heidelberg: Berlin, Heidelberg. p. 163-177.

186. Shi, Z., et al., *Lead-Free Organic-Inorganic Hybrid Perovskites for Photovoltaic Applications: Recent Advances and Perspectives.* Adv Mater, 2017. **29**(16).

187. Eames, C., et al., *Ionic transport in hybrid lead iodide perovskite solar cells.* Nature Communications, 2015. **6**(1): p. 7497.

188. Wark, S.E., C.H. Hsia, and D.H. Son, *Effects of ion solvation and volume change of reaction on the equilibrium and morphology in cation-exchange reaction of nanocrystals.* J Am Chem Soc, 2008. **130**(29): p. 9550-5.

189. Rivest, J.B. and P.K. Jain, *Cation exchange on the nanoscale: an emerging technique for new material synthesis, device fabrication, and chemical sensing.* Chemical Society Reviews, 2013. **42**(1): p. 89-96.

190. Koliogiorgos, A., et al., *Electronic and Optical Properties of Ultrasmall ABX(3) (A = Cs, CH(3)NH(3)/B = Ge, Pb, Sn, Ca, Sr/X = Cl, Br, I) Perovskite Quantum Dots.* ACS omega, 2018. **3**(12): p. 18917-18924.

191. Atkin, R., et al., *Structure and dynamics of the interfacial layer between ionic liquids and electrode materials.* Journal of Molecular Liquids, 2014. **192**: p. 44-54.

192. Cho, G., et al., *Ion exchange: an advanced synthetic method for complex nanoparticles.* Nano Convergence, 2019. **6**(1): p. 17.

193. Wang, X.-D., et al., *Recent Advances in Halide Perovskite Single-Crystal Thin Films: Fabrication Methods and Optoelectronic Applications.* Solar RRL, 2019. **3**(4): p. 1800294.

194. Xu, X. and X. Wang, *Perovskite Nano-Heterojunctions: Synthesis, Structures, Properties, Challenges, and Prospects.* Small Structures, 2020. **1**(1): p. 2000009.

195. Nayak, P.K., et al., *Mechanism for rapid growth of organic–inorganic halide perovskite crystals.* Nature Communications, 2016. **7**(1): p. 13303.

196. Dang, Y., et al., *Bulk crystal growth of hybrid perovskite material CH3NH3PbI3.* CrystEngComm, 2015. **17**(3): p. 665-670.

197. Saidaminov, M.I., et al., *Retrograde solubility of formamidinium and methylammonium lead halide perovskites enabling rapid single crystal growth.* Chemical Communications, 2015. **51**(100): p. 17658-17661.

198. Saidaminov, M.I., et al., *High-quality bulk hybrid perovskite single crystals within minutes by inverse temperature crystallization.* Nat Commun, 2015. **6**: p. 7586.

199. Peng, W., et al., *Solution-Grown Monocrystalline Hybrid Perovskite Films for Hole-Transporter-Free Solar Cells.* Adv Mater, 2016. **28**(17): p. 3383-90.

200. Yao, F., et al., *Room-temperature liquid diffused separation induced crystallization for high-quality perovskite single crystals.* Nature Communications, 2020. **11**(1): p. 1194.

201. Liu, Y., et al., *Low-temperature-gradient crystallization for multi-inch high-quality perovskite single crystals for record performance photodetectors.* Materials Today, 2019. **22**: p. 67-75.

202. Kadro, J.M., et al., *Facile route to freestanding CH3NH3PbI3 crystals using inverse solubility.* Scientific reports, 2015. **5**: p. 11654-11654.

203. Bi, D., et al., *Effect of Different Hole Transport Materials on Recombination in CH3NH3PbI3 Perovskite-Sensitized Mesoscopic Solar Cells.* The Journal of Physical Chemistry Letters, 2013. **4**(9): p. 1532-1536.

204. Rao, H.-S., et al., *A micron-scale laminar MAPbBr3 single crystal for an efficient and stable perovskite solar cell.* Chemical Communications, 2017. **53**(37): p. 5163-5166.

205. Rao, H.-S., et al., *In Situ Growth of 120 cm2 CH3NH3PbBr3 Perovskite Crystal Film on FTO Glass for Narrowband-Photodetectors.* Advanced Materials, 2017. **29**(16): p. 1602639.

206. Cheng, Z., et al., *High-Performance Planar-Type Ultraviolet Photodetector Based on High-Quality CH3NH3PbCl3 Perovskite Single Crystals.* ACS Applied Materials & Interfaces, 2019. **11**(37): p. 34144-34150.

207. Li, L., et al., *Space-confined growth of metal halide perovskite crystal films.* Nano Research, 2021. **14**(6): p. 1609-1624.

208. Chen, Y., et al., *Structure and Growth Control of Organic–Inorganic Halide Perovskites for Optoelectronics: From Polycrystalline Films to Single Crystals.* Advanced Science, 2016. **3**(4): p. 1500392.

209. K. Rao, M., et al., *Review on persistent challenges of perovskite solar cells' stability.* Solar Energy, 2021. **218**: p. 469-491.

210. Di, H., et al., *Improving the crystallinity of CH3NH4PbBr3 single crystal thin films via controlling the evaporation of methylamine.* Thin Solid Films, 2021. **720**: p. 138519.

211. Ding, J., et al., *Controlled growth of MAPbBr3 single crystal: understanding the growth morphologies of vicinal hillocks on (100) facet to form perfect cubes.* Journal of Materials Science, 2017. **52**(13): p. 7907-7916.

212. Yaffe, M.J. and J.A. Rowlands, *X-ray detectors for digital radiography.* Physics in Medicine and Biology, 1997. **42**(1): p. 1-39.

213. Cowen, A.R., S.M. Kengyelics, and A.G. Davies, *Solid-state, flat-panel, digital radiography detectors and their physical imaging characteristics.* Clin Radiol, 2008. **63**(5): p. 487-98.

214. Wei, H., et al., *Sensitive X-ray detectors made of methylammonium lead tribromide perovskite single crystals.* Nature Photonics, 2016. **10**(5): p. 333-339.

215. Hoheisel, M., *Review of medical imaging with emphasis on X-ray detectors.* Nuclear Instruments and Methods in Physics Research Section A: Accelerators, Spectrometers, Detectors and Associated Equipment, 2006. **563**(1): p. 215-224.

216. Yakunin, S., et al., *Detection of X-ray photons by solution-processed organic-inorganic perovskites.* Nat Photonics, 2015. **9**(7): p. 444-449.

217. Spina, M., et al., *Controlled growth of CH3NH3PbI3 nanowires in arrays ofopen nanofluidic channels.* Scientific Reports, 2016. **6**(1): p. 19834.

218. Dualeh, A., et al., *Effect of Annealing Temperature on Film Morphology of Organic–Inorganic Hybrid Pervoskite Solid-State Solar Cells.* Advanced Functional Materials, 2014. **24**(21): p. 3250-3258.

219. Liu, Y., et al., *Thinness- and Shape-Controlled Growth for Ultrathin Single-Crystalline Perovskite Wafers for Mass Production of Superior Photoelectronic Devices.* Advanced Materials, 2016. **28**(41): p. 9204-9209.

220. Liu, Y., et al., *Thinness- and Shape-Controlled Growth for Ultrathin Single-Crystalline Perovskite Wafers for Mass Production of Superior Photoelectronic Devices.* Adv Mater, 2016. **28**(41): p. 9204-9209.

221. Lalitha, M. and S. Lakshmipathi, *Interface energetics of [Emim]+[X]− and [Bmim]+[X]− (X=BF4, Cl, PF6, TfO, Tf2N) based ionic liquids on graphene, defective graphene, and graphyne surfaces.* Journal of Molecular Liquids, 2017. **236**: p. 124-134.

222. Wasserscheid, P., *Volatile times for ionic liquids.* Nature, 2006. **439**(7078): p. 797-797.

223. Aliaga, C., C.S. Santos, and S. Baldelli, *Surface chemistry of room-temperature ionic liquids.* Physical Chemistry Chemical Physics, 2007. **9**(28): p. 3683-3700.

224. Burgess, S., et al., *Ultra-Low kV EDS – A New Approach to Improved Spatial Resolution, Surface Sensitivity, and Light Element Compositional Imaging and Analysis in the SEM.* Microscopy Today, 2017. **25**(2): p. 20-29.

225. Xue, J., R. Wang, and Y. Yang, *The surface of halide perovskites from nano to bulk.* Nature Reviews Materials, 2020. **5**(11): p. 809-827.

226. ChemicalBook, *CAS database*.

227. Wehrenfennig, C., et al., *Charge carrier recombination channels in the low-temperature phase of organic-inorganic lead halide perovskite thin films.* APL Materials, 2014. **2**(8): p. 081513.

228. Bari, M., et al., *Room-temperature synthesis, growth mechanisms and opto-electronic properties of organic–inorganic halide perovskite CH3NH3PbX3 (X = I, Br, and Cl) single crystals.* CrystEngComm, 2021. **23**(18): p. 3326-3339.